# Experimental and numerical investigations on aircraft icing at mixed phase conditions

A. Baumert, S. Bansmer, P. Trontin, P. Villedieu

# Experimental and numerical investigations on aircraft icing at mixed phase conditions

A. Baumert [a,*,1], S. Bansmer [a,**,2], P. Trontin [b,**,3], P. Villedieu [b,4]

[a] *Institute of Fluid Mechanics, Technische Universität Braunschweig, Hermann-Blenk-Str. 37, Braunschweig, Germany*
[b] *ONERA – The French Aerospace Lab, F-31055 Toulouse, France*

Since the beginning of civil aviation, icing is a severe weather hazard for aircraft operation. In this con-text, the phenomenon of ice crystal icing has been identified as a risk for flight safety in the recent past. Ice crystals can accrete on warm components such as heated stagnation pressure probes and engine com-pressor blades. Liquid melt water or additional liquid droplets in the icing cloud enable the ice particles to stick to the component surface and to form a cohesive ice accretion layer. In this paper, we present results of comprehensive icing wind tunnel tests on ice crystal ice accretion together with results of complemen-tary simulations by means of the ONERA icing code IGLOO2D. The experiments show a strong influence of ambient temperature on the icing process. In agreement with literature findings, ice particle sticking abil-ity can be correlated with the ice cloud composition. Correlations between accretion shape and growth rate have been identified. IGLOO2D separates accretion abrasion by particle impact from the efficiency with which those particles stick to the deposit. Comparisons of computational and experimental results indicate that this sticking efficiency has the greatest effect on ice shapes at low Mach numbers, at least for the particle sizes and conditions used in the experiments. The experimental and numerical findings of this study can be considered as complementary to existing knowledge on ice crystal icing. Therefore, the experimental results are provided to an international benchmark of test cases for icing code validation.

## 1. Introduction

Since the beginning of aeronautical engineering, aircraft icing has been a great issue to flight safety. Consequently, research on this topic is ongoing for decades. Most of these research activities are dedicated to supercooled droplet icing which can be addressed as the primary icing hazard for aircraft in flight [1,2]. Supercooled droplets appear in the earth atmosphere at temperatures in the range of 0 to −40 °C. These liquid droplets can be considered as thermodynamically metastable, a phase change to solid state can be initiated by local mechanical disturbances, for example by collision with an aircraft passing a cloud of supercooled droplets. Droplet freezing on the aircraft fuselage, wings and engine intakes causes a great reduction of flight performance. Additional weight and increased drag go along with lift losses and result in severe danger for aircraft operation.

Beside supercooled droplet icing (SDI), another icing mechanism called ice crystal icing (ICI) has to be considered as a severe risk for flight safety [3]. Dense clouds of fully frozen ice crystals can be found in the vicinity of mesoscale convective cloud systems (MCS), mostly in tropical regions [4]. At flight altitude, high concentrations of particular small ice crystals are found which can rarely be detected by current on-board radar technology. Ice crystal concentrations are quantified by the ice water content (IWC) similar to the liquid water content (LWC) of supercooled droplet clouds. The liquid water content is defined as the ratio of cumulative liquid droplet mass to the surrounding volume of air. At atmospheric temperatures above −40 °C, mixed phase clouds consisting of solid ice particles and liquid droplets can appear. The overall water mass of these clouds is quantified by the total water content TWC which is the sum of LWC and IWC and water vapor.

This paper is dedicated to mixed phase icing. Mixed phase clouds generally appear below the flight level of civil aircraft and

* Corresponding author.
** Principal corresponding author.
*E-mail addresses:* a.baumert@tu-braunschweig.de (A. Baumert), pierre.trontin@onera.fr (P. Trontin).
[1] Research assistant.
[2] Research associate.
[3] Research engineer.
[4] Research director.

**Nomenclature**

| | |
|---|---|
| $\alpha_0$ | accretion efficiency |
| $\beta_0$ | stagnation point collection efficiency |
| $\epsilon_s$ | ice particle sticking efficiency |
| $\rho_{acc}$ | density [kg/m$^3$] |
| $\varphi_0$ | accretion tip angle [°] |
| $f_l$ | accretion surface total liquid fraction |
| $\dot{m}_f$ | freezing mass rate [kg/(s · m$^2$)] |
| $\dot{m}_{dep}$ | deposition mass flux [kg/(s · m$^2$)] |
| $\dot{m}_{imp}$ | impinging mass flux [kg/(s · m$^2$)] |
| $m_r$ | melting ratio |
| $M$ | Mach number |
| $t_L$ | accretion leading edge thickness [mm] |
| $\dot{t}_L$ | accretion growth rate [mm/s] |
| $T_\infty$ | static temperature [°C] |
| $T_{wb}$ | wet bulb temperature [°C] |
| $U_\infty$ | free stream velocity [m/s] |
| $y_l$ | accretion surface liquid mass fraction |
| *CIRA* | Centralo Italiano Ricerche Aerospaziali |
| *HAIC* | High Altitude Ice Crystals |
| *ICI* | Ice Crystal Icing |
| *IGLOO2D* | ONERA 2D icing suite |
| *IGS* | Ice Crystal Generation and Conveyance System |
| *IKP* | Isokinetic Probe |
| *IWC* | Ice Water Content |
| *IWT* | Icing Wind Tunnel |
| *LWC* | Liquid Water Content |
| *MCS* | Mesoscale Convective System |
| *MVD* | Medium Volume Diameter |
| *MMD* | Medium Mass Diameter |
| *NASA* | National Aeronautics and Space Administration |
| *NRC* | National Research Council of Canada |
| *ONERA* | Office National d'Etudes et de Recherches Aerospatiales |
| *PSL* | Propulsion System Laboratory |
| *RATFac* | Research Altitude Test Facility |
| *SDI* | Supercooled Droplet Icing |
| *SLD* | Supercooled Large Droplet |
| *TUBS* | Technische Universität Braunschweig |
| *TWC* | Total Water Content |

are strongly avoided because of increased icing severity. However, they might be unavoidable to pass during climb or descend.

Beside atmospheric clouds, mixed phase conditions can also occur around warm aircraft assemblies, such as heated stagnation pressure probes and engine compressor blades. Convective heating and particle impact on heated surfaces can cause the ice crystals to partially melt. The liquid phase enables the particles to stick on probes or engine stator blades, as soon as the concerned component has cooled down to freezing temperature upon particle impact. The amount of liquid that is involved in ice crystal icing is characterized by the melting ratio $m_r$, which is defined as the ratio of liquid to total water content:

$$m_r = \frac{\eta_m \cdot IWC + LWC}{TWC} \tag{1}$$

$\eta_m$ is the ice crystal melting ratio which quantifies the melt water of initially solid ice crystals. The term 'melting ratio' is also used in the present study, even if the liquid phase does origin from supplemental water supply and not from ice particle melting ($\eta_m = 0$). In contrast to mixed phase conditions, solid ice particles bounce off cold surfaces which is why glaciated clouds cause no danger of wing or fuselage icing.

Icing of aircraft probes can cause false flight parameters displayed inside the cockpit. In case of aircraft engines, ice accretion related to ice crystal icing is observed to appear at the outer regions of the low pressure compressor stator blades [5]. Ice accretion inside the compressor causes flow blockage, forcing the compressor to operate towards stall conditions. The compressor encounters a decay in rotational speed resulting in significant thrust losses (rollback event) [6]. Moreover, total engine flame out may appear if great masses of accumulated ice are shed into the combustor. Atmospheric mixed phase clouds can cause icing of the outer aircraft surface similar to supercooled droplet icing but usually of enhanced severity.

Recent flight campaigns conducted in the course of the HAIC project have yielded total water contents up to 4 g/m$^3$ in MCSs at flight altitude [7]. TWCs up to 4 g/m$^3$ are reasonable for mixed phase clouds at atmospheric temperatures between −40 and 0 °C [8]. Atmospheric ice crystal clouds have been observed to feature median mass diameters in the range of 300–800 μm [9]. Inside the engine, ice particles are expected to be significantly smaller (MMD of 20–40 μm) because the particles get fragmented inside the fan and first compressor stages [10]. Centrifuging increases the particle concentration (TWC) near the compressor outer casing. Total water contents four times higher than the atmospheric TWC are expected to cause local ice accretion around the stator blade roots [10].

Fundamental research on ice crystal icing has been sparked by the comprehensive paper of Mason et al. on engine icing from 2006 [3]. Most of these research activities have been performed from an experimental point of view by the National Research Council of Canada (NRC) and NASA [11–13]. A great variety of experiments has been performed at the NRC Research Altitude Test Facility (RATFac) [14,15]. In the following, selected research findings of NRC studies are presented and compared to the results of this study in subsequent chapters.

At current state, the NRC studies at RATFac have focused on investigations of ice accretion behaviour of generic test articles depending on aerothermal and icing cloud conditions. The NRC studies have shown that ice crystal icing inside an engine is limited to a characteristic range of melting ratios. Significant ice accretions have been observed for melting ratios ranging from 5 to 35 percent. A plateau of constant icing severity has been reported which drastically decreases at its left and right boundary, see Fig. 1. It has been concluded that at low melting ratios not enough liquid water is present to enable the ice particles to effectively stick to the model surface. At the right boundary of the plateau, the amount

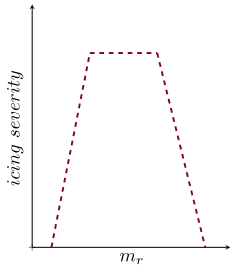


**Fig. 1.** Mixed phase icing: Icing severity vs. melting ratio.

of liquid is too high to form a cohesive composite which resists abrasion effects of impinging particles. Insufficient cooling of the substrate may contribute to accretion reductions at the right boundary. The term 'erosion' has been introduced to describe accretion abrasion by particle impact. In this context a strong influence of ice particle sizes and impact velocities has been reported. The icing regime narrows for increased particle speeds and sizes. The right end of the plateau moves towards lower melting ratios because of increased erosion effects and accretion melting by dissipating of kinetic energy of impinging particles [16–18]. Since liquid phase is adjusted by particle melting, higher melting ratios also correlate with an increase of ambient temperature and thus convective heating of the ice accretion in the NRC studies [18].

Ice accretions at mixed phase conditions are typically wedge-shaped. Fig. 2 shows ice accretion shapes on a cylinder model deduced from NRC studies at RATFac [18]. The experiments have been conducted at Mach numbers of 0.25 and 0.4, the ice cloud melting ratio has been varied at a constant total water content of 6 g/m$^3$. All images in Fig. 2 represent steady state conditions that means the accretion shape does not change in time, even being further exposed to a mixed phase cloud. At M = 0.25 severe icing can be observed for a melting ratio of 0.14 with significantly reduced accretion at $m_r = 0.31$ indicating the right end of the icing envelope according to Fig. 1. At M = 0.4 only very little accretion occurs for $m_r = 0.14$ compared to M = 0.25. The right end of the icing plateau also shifts towards a lower melting ratio of about 0.21.

Mach numbers up to 0.6 are reached in high TWC regions of engine compressors. Currie et al. have performed ice accretion tests on a hemisphere model and a wedge airfoil at M = 0.65 [17]. Ice accretions only formed when extremely small ice particles with an MMD of about 30 μm were injected into the test cell. These results are in agreement with the expectation of very small ice particles inside the engine due to particle break up in the fan stage.

As indicated above, the ice accretion process is very sensitive to melting ratio. At RATFac, the liquid phase of the cloud is generated by particle melting. Thus, the wet bulb temperature $T_{wb}$ of the airflow has been identified as a suitable parameter to characterize aerothermal cloud conditions. The wet bulb temperature is defined as the lowest temperature a sample of air can reach as it passes a liquid layer on an adiabatic surface. It actually corresponds to the steady state film temperature when evaporative cooling and convective heating by the airflow are in balance. Applied to icing conditions, wet bulb temperatures above 0 °C cause ice melting while $T_{wb} < 0$ affects film freezing [16]. Currie et al. have shown that the primary effect of $T_{wb}$ on ice accretion growth is its influence on the cloud melting ratio [12].

NRC studies have also shown that icing severity depends on total water content, at least at low Mach numbers. Fig. 3 shows ice accretion on the cylinder model at similar conditions compared to Fig. 2(a) except that TWC has been increased to 12 g/m$^3$. A very long accretion with a sharp tip angle has developed, which shed from the test article before steady state conditions had been reached. Similar tests at M = 0.4 have also shown an increase in icing severity with TWC but not as significant as for M = 0.25. Ice

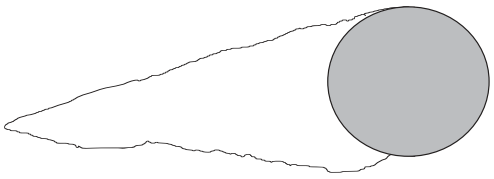

**Fig. 3.** NRC experiments: Mixed phase ice accretion on a crowned cylinder, $TWC \approx 12$ g/m$^3$, $M = 0.25, m_r$ in optimum icing regime, with permission of Currie et al. [18].

accretion shedding is a frequently observed phenomenon for mixed phase icing at wet bulb temperatures above the freezing point. For $T_{wb} > 0$ °C the ice accretion does not strongly adhere to the substrate surface and can get dragged by the ambient airflow. In case of engine icing, subsequent compressor blades may sustain abrasive damages by impacting ice masses shed upstream. Moreover, engine flame out is possible if great masses of ice instantly enter the combustor. Experimental investigations on accretion shedding have been conducted at NRC [19,16,20]. Complementary numerical studies have been performed at TU Darmstadt. A shedding criterion has been determined [21] based on the amount of liquid at the interface between ice accretion and substrate surface.

The findings discussed above refer to engine conditions characterized by wet bulb temperatures above the freezing point. Mixed phase icing below 0 °C can be relevant for wing icing as an aircraft passes the mixed phase region of a convective cloud but also for inside engine conditions if a mixed phase cloud is ingested. It is also possible that ice particles melt upon impact on compressor blades that are heated for deicing purpose. At mixed phase conditions below the freezing point no right end of the icing envelope in Fig. 1 exists. The icing process changes to supercooled droplet icing at $m_r = 1$.

Studies on ice accretion at sub zero temperatures have been performed recently at RATFac by means of a hemispheric test model [17]. The tests have shown enhanced icing severity for decreasing temperatures below the freezing point. Moreover, the experiments have yielded rather untypical ice accretions of a mushroom-type shape, see Fig. 4(a). The more normal tangential transition from a conical accretion to the test article was only observed at $T_{wb}$ slightly below freezing and a moderate melting ratio of 0.2., cf. Fig. 4(b).

Further mixed phase tests below 0 °C have been performed at the COX Icing research tunnel [22,23]. Ice accretion tests have been performed on a NACA 0012 airfoil at rather low total water contents in the range of 0.3–1.4 g/m$^3$ and at a low Mach number of 0.165. Temperatures have been varied between −7 °C and −12 °C, melting ratios have been adjusted in the range of 0.3 and 0.7. The tests have yielded different kinds of ice accretion depending on the cloud conditions and temperatures. At the higher temperature of −7 °C, irregular ice accretions covered by liquid phase have been observed, see Fig. 5(a). In contrast, very smooth and dry accretions have been obtained at −12 °C, cf. Fig. 5(b).

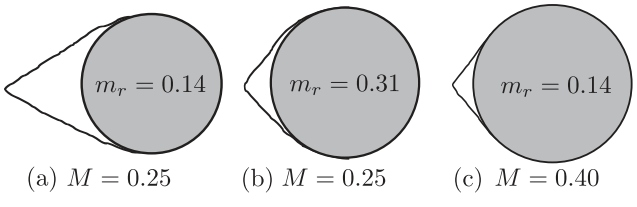


**Fig. 2.** NRC experiments: Mixed phase ice accretion on a crowned cylinder, $TWC \approx 6$ g/m$^3$ and $T_{wb}$ variation in the range of 1–5.5 °C, with permission of Currie et al. [18].

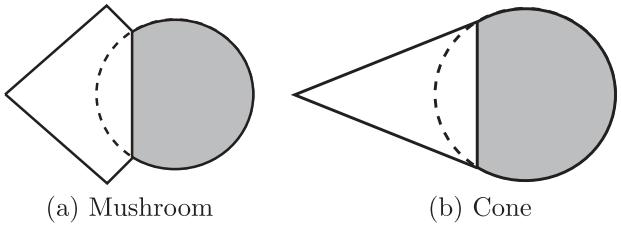


**Fig. 4.** NRC experiments: Accretion shapes obtained for mixed phase icing on a sphere at wet bulb temperatures below freezing, with permission of Currie et al. [17].

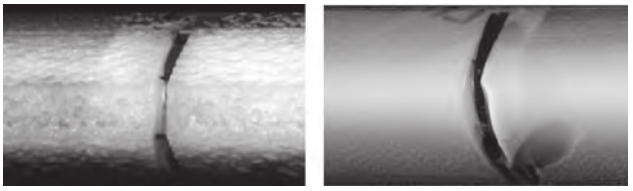

(a) $m_r = 0.5$, $T_\infty = -7^\circ\ C$ (b) $m_r = 0.3$, $T_\infty = -12.5^\circ\ C$

**Fig. 5.** COX and NASA experiments: Mixed phase ice accretion of a NACA 0012 airfoil, $TWC = 1 \ldots 1.4\ \mathrm{g/m^3}$ and $U_\infty = 53.6$ m/s, with permission of Al-Khalil et al. [22].

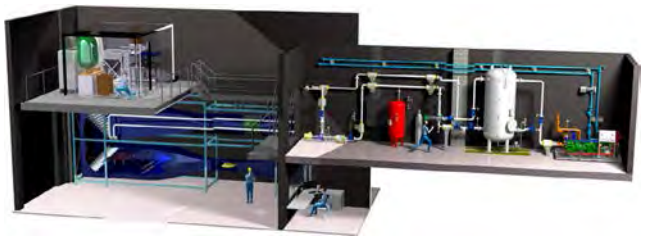

**Fig. 6.** TU Braunschweig Icing Wind Tunnel facility [9].

The authors thus differentiated between glaze and rime ice conditions according to terms generally used in the context of supercooled droplet icing.

Apart from ice accretion tests, extensive ice particle impact studies have been conducted by Hauk et al. [24,25]. Hauk investigated ice particle impact on solid heated and unheated surfaces as well as on surfaces covered by a liquid layer. He observed dependencies of particle breakup on impact velocity and particle size. Roisman and Tropea derived a mathematical theory on the impact behaviour of spherical ice particles based on Hauk's studies [26]. The rebound behaviour of ice particle fragments observed in Hauks studies has been respected in ONERA's IGLOO2D code to simulate secondary particle trajectories, cf. Section 4.1.

To finish this overview about experimental studies on ice crystal icing, NASA's research activities on the topic shall be pointed out. At the Propulsion System Laboratory (PSL) full scale engine tests can be performed at ice particle cloud conditions [27]. PSL is an open circuit wind tunnel equipped with cameras and a wide range of instruments for measuring icing conditions and changes in engine performance due to ice build up. Liquid droplets are injected upstream of the engine and forced to freeze out to generate ice particles [28]. Results can be compared to service events and also be used to validate numerical engine icing models, [6,29]. Reference [5] reports ice crystal tests of a Honeywell ALF502R-5 engine in PSL.

Regarding modelling and numerical simulation dedicated to ice accretion, the first extensions of the original Messinger model [30] to take into account ice particle impingement in the balance equation have been developed by Wright [31], Habashi [32], Ríos Pabón [33] and Oliver [34]. Multilayer and film models have been extended to ice crystal icing by Chauvin et al. [35,36] and Wright [31]. Notably, shedding of ice layers which is common in warm icing conditions is typically not predicted by the classical Messinger models but is taken into account in Bennani [37,38] or Kintea [39]. The European project HAIC has been the opportunity for existing icing tools to extend their capabilities with ice crystal modelling [40,41].

## 2. Experimental setup

### 2.1. Icing Wind Tunnel Braunschweig

The experimental results presented in this paper have been carried out in the course of two test campaigns at the TU Braunschweig Icing Wind Tunnel (IWT) facility. A comprehensive description of the design, construction and commissioning of the facility is given by Bansmer et al. [9].

The overall facility is illustrated in Fig. 6 where the wind tunnel is highlighted in blue[5] colour. It is a closed loop wind tunnel, air speeds up to 40 m/s can be adjusted inside the test section, which features a cross sectional area of 500 × 500 mm. The wind tunnel can be operated in a static temperature range of −20 °C to 30 °C. Temperature adjustment is possible by means of an external refrigeration system, which is shown in the right side of Fig. 6. The refrigeration system provides cooling power of up to 80 kW to a heat exchanger implemented into the wind tunnel.

A conceptual sketch of the icing wind tunnel facility is shown in Fig. 7. Again, the icing wind tunnel is highlighted in blue colour. By means of a spray bar system (o), liquid water can be atomized at the entry of the wind tunnel nozzle to generate supercooled droplet clouds. To simulate glaciated and mixed phase icing conditions, solid ice particles can additionally be injected into the tunnel. Ice particles are generated and supplied by an external ice crystal generation and conveyance system (IGS). The IGS is placed on an extra floor, shown on the upper side of Fig. 6. The main component of the IGS is a cooling chamber (a) in which ice particle generation and dosing takes place. Ice crystal generation is realized by cloud chamber technology (b). The ice particles are generated and stored (c) prior to an experiment. During a test run the particles are dosed (i) and sieved (h) by custom made machinery to adjust the ice particle massflow supplied to the IWT. The ice particles are pneumatically blown into the wind tunnel upstream of the spraybar system. Detailed information about ice particle generation and mixed phase capabilities are given by Baumert et al. in [42,43].

The ice particle generation and conveyance system allows to adjust ice water contents in the range of 3–20 $\mathrm{g/m^3}$ inside the test section. These values correspond to total water contents expected inside engine compressors, see Section 1. Ice particle cloud calibration has been performed by means of the Cranfield University Isokinetic probe, the CIRA High Speed Imaging probe and a particle collecting tube system [9,43]. The cloud is characterized by a median mass diameter (MMD = $D_{50}$) of 80 µm. $D_{10}$ and $D_{90}$, representing 10% and 90% of the cumulative mass are 20 µm and 220 µm respectively. Liquid water contents can be set in the range of 1.4–3.4 $\mathrm{g/m^3}$ for wind tunnel speeds of 40 m/s. The droplet cloud has been calibrated by means of the Cranfield University Isokinetic Probe, the CIRA High Speed Imaging- and Phase Doppler Interferometry Probe [9,43]. Inside the test section the droplet cloud median volume diameter (MVD) is about 80 µm. IWC and LWC have been determined on the test section centerline. An uncertainty of ±10% is stated for the Cranfield University Isokinetic probe.

### 2.2. Test matrix

The operational range of the spraybar system and the IGS allows to adjust a broad variety of mixed phase cloud conditions. Fig. 8 illustrates the selection of test conditions for this study. The melting ratio $m_r$ has been varied between 0 and 0.6 for mixed phase cloud conditions. The total water content *TWC* cannot be maintained constant in this range because the maximum LWC of 3.4 $\mathrm{g/m^3}$ is reached at $m_r = 0.28$. Consequently, the IWC has to be decreased to adjust higher melting ratios. As illustrated in

[5] For interpretation of color in Fig. 6, the reader is referred to the web version of this article.

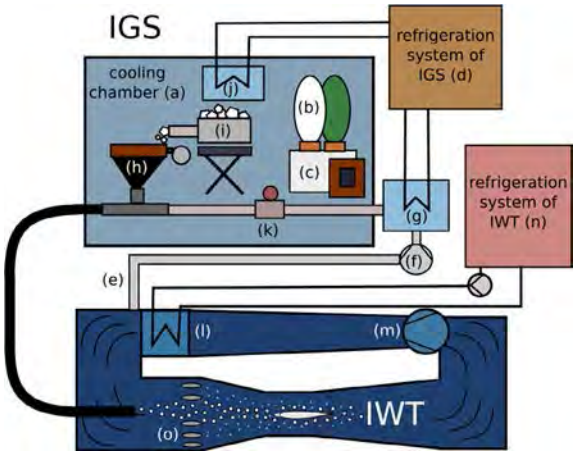


**Fig. 7.** Simplified flow chart of IWT and IGS [43].

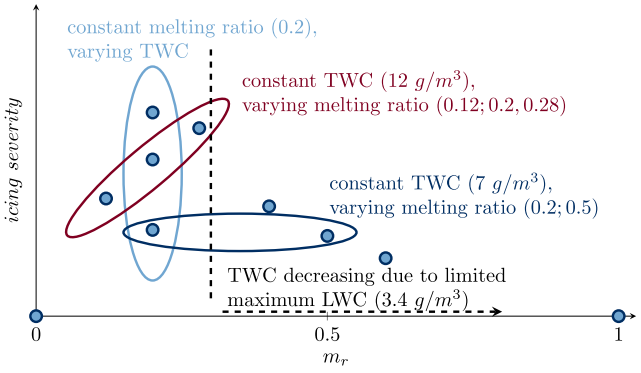


**Fig. 8.** Strategy of test point selection.

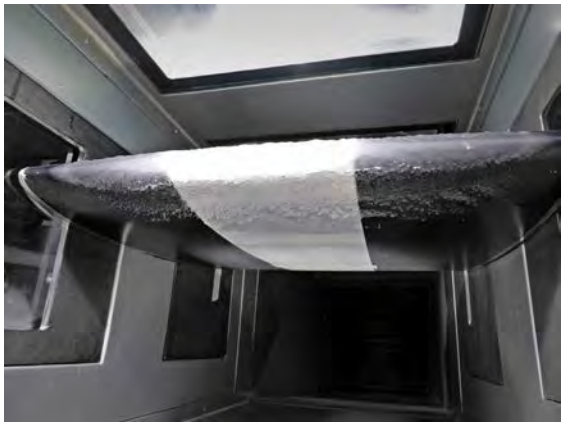

**Fig. 9.** NACA 0012 airfoil covered with ice layer inside the IWT test section.

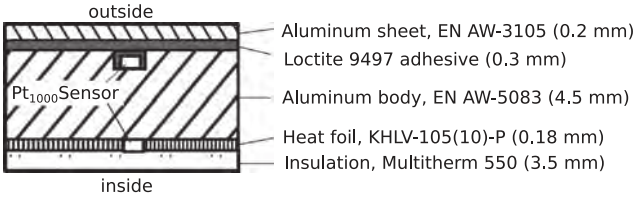


**Fig. 10.** Internal instrumentation of the test articles.

Fig. 8, the *TWC* is kept constant at 12 g/m$^3$ for melting ratios in the range of 0.12–0.28. To investigate the effect of total water content variation on the ice accretion process, the TWC has been varied between 7 and 17 g/m$^3$ at a constant melting ration of 0.2. In case of $TWC = 7$ g/m$^3$ comparisons at rather constant total water contents are possible to cloud conditions of $m_r = 0.5$ where the TWC is set to 6.8 g/m$^3$. Ice accretion tests have been performed at static temperatures of 0 °C, − 5 °C and −15 °C in this study. At $T_\infty = 0$ °C and $T_\infty = -5$ °C all test points of Fig. 8 have been investigated. In the case of $T_\infty = -15$ °C icing tests have only performed at melting ratios of 0.12, 0.28 and 1. It has to be pointed out that for all test conditions relative humidity was close to saturation so that the static temperature $T_\infty$ is equal to the wet bulb temperature $T_{wb}$.

Based on weightings of ice particle deposits on the sieving machine of the IGS, the accuracy of TWC can be estimated as ±15% around the target value. For most of the tests performed, the accuracy is in the range of ±5%. Several tests have been repeated at the same cloud conditions and the agreement in accretion shape was very good. Total temperature can be set with a temporal uniformity of 0.5 °C. Further deviations of centerline temperature from the target value appear due to imperfect mixing of the particle laden jet with the ambient airflow. This effect can be assessed as several tenth degree Celsius.

### 2.3. Test articles

Two test articles have been designed and manufactured for mixed phase ice accretion studies. One of these models is a NACA 0012 airfoil of 500 mm chord length, which is shown in Fig. 9.

The model features a modular design, the center element is manufactured from aluminum while the two outer elements are made of Necuron, a synthetic material of low thermal conductivity. The aluminum element is equipped with internal heat foils and pt-1000 resistor thermometers, which are placed directly underneath the airfoil surface. The heat foils allow to investigate the effect of heat introduction into the ice accretion. This aspect is not part of the presented work. Fig. 10 illustrates the internal model design and instrumentation. In addition to the airfoil, a cylinder model with similar internal instrumentation has been manufactured. The cylinder has a diameter of 60 mm which corresponds to the maximum thickness of the airfoil. In contrast to the airfoil, the cylinder is connected to a supporting rod and does not cover the total horizontal extension of the test section, see Fig. 11, top right. As illustrated in the left image of Fig. 11, also the cylinder model features a modular design. The front shell is made of aluminum and includes temperature sensors and heat foils. The white layer is an insulation composite which prevents heat emission of the heat foils to the interior of the cylinder. The back shell is made of polyvinylchloride and prevents heat absorption due to its low thermal conductivity.

**Fig. 11.** Design and instrumentation of the test articles.

*2.4. Optical setup*

The main objective of the ice accretion studies presented in this paper was to investigate ice accretion growth depending on the ambient icing conditions. To monitor the accretion process, four cameras have been installed around the test section. Hd- and full-hd video sequences of the accretion procedure have been captured as well as high resolution images of the final ice accretion shape and structure.

Further high speed investigations on ice particle impact at mixed phase conditions have been performed in a complementary study to this work [44].

Fig. 12 shows the camera arrangement of the accretion studies. Videos are taken by the top-, side- and bottom view camera. The top- and side view video material allows to quantitatively evaluate the ice accretion process. The bottom view offers a third perspective for qualitative observations. The front side camera takes frequent images during a test run and allows to investigate the macroscopic surface structure of the ice accretion. In addition to the four cameras, a laser with a system of cylindrical and spherical lenses is mounted on top of the test section. The laser, type Pegasus PL.PF.532, produces a constant light sheet vertically across the test section.

An illustration of the optical setup is shown in Fig. 13. The top and side view cameras are oriented perpendicular to the flow and focused on the symmetry planes of the airfoil. The optical axis of the side view camera is shifted 25 mm to the front of the leading edge of the airfoil. This arrangement avoids that the ice accretion at centerline position is hidden by ice accretion between focal plane and camera. The laser sheet is aligned congruent to the focal plane of the side view camera and illuminates the ice accretion contour.

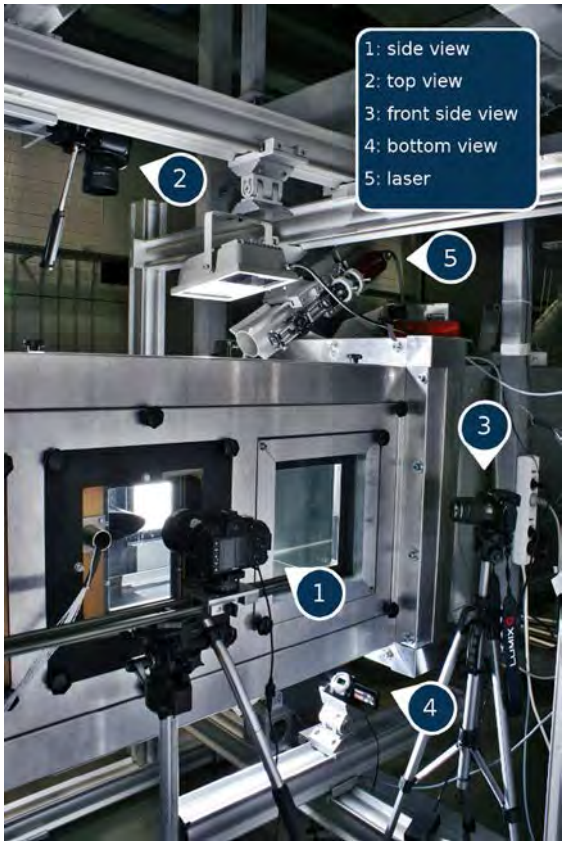


**Fig. 12.** Experimental setup.

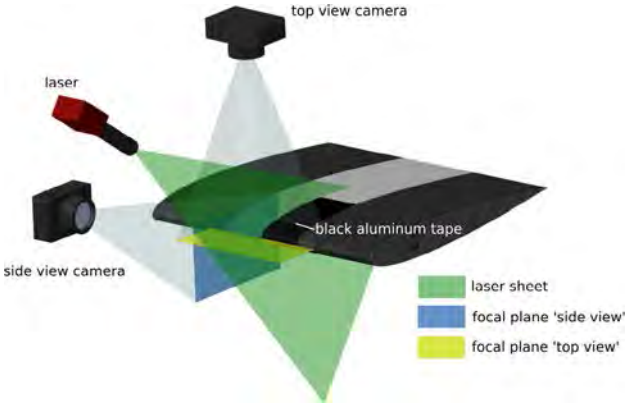


**Fig. 13.** Adjustment of the laser, top- and side view camera.

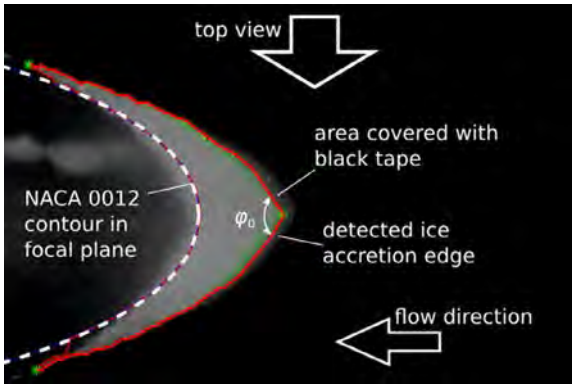


**Fig. 14.** Side view image of ice accretion; note that in this image airflow and ice particles are coming from the right.

Ice accretion detection based on top view and side view video material is realized by a custom made matlab tool. Based on a gradient criteria of greyscale image intensity the ice accretion is detected. The laser sheet allows to highlight the ice accretion contour at centerline position. To further increase the image intensity gradient around the centerline accretion contour, the test article is covered with black aluminum tape. The tape is fixed behind the focal plane of the camera, see Fig. 13. Light reflections of the airfoil surface behind the focal plane are reduced by the black tape to enhance the light intensity gradient around the centerline accretion contour.

A characteristic side view camera image is shown in Fig. 14. The ice accretion faces air- and particle flow from the right according to the camera orientation in Figs. 12 and 13. The contour of the NACA 0012 airfoil at centerline position is highlighted by a dashed white line. It is determined by the accretion detection algorithm based on a prior image of a calibration plate. The red line highlights the detected accretion shape and is congruent with the laser sheet outline. Due to the use of black aluminum tape, the ice accretion brightness behind the focal plane is significantly reduced which makes the detection algorithm work much more efficiently and reliably.

The top view camera offers an additional option for ice accretion detection. As the inside wall of the test section is covered with a black foil, a good contrast is given for permanent ice accretion detection, see Fig. 15. Based on a prior calibration, the detection algorithm scans the 2D top view ice accretion shape and evaluates the centerline ice accretion thickness. Compared to the side view perspective the top view evaluation is less error-prone. Thus, the results shown in the following chapters are based on evaluation

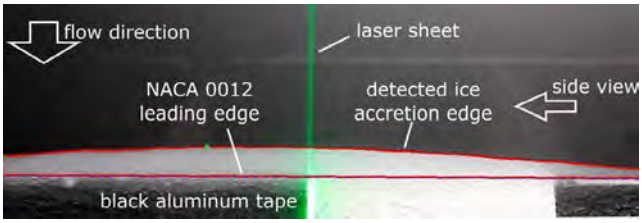


**Fig. 15.** Top view image of ice accretion.

of the top view camera. This concerns accretion growth histories and accretion efficiencies. The 2D side view accretion shapes used for comparison to the numerical results have been ensured to be properly detected.

All cameras are switched on sequentially before an experiment. To synchronize the video material, a flash is triggered prior to the test run which is clearly detected by the ice accretion detection algorithm. Ice accretion tests require steady state icing cloud conditions. Initiation times between 30 and 60 s have been identified for the droplet and ice particle cloud in the course of the wind tunnel calibration. To respect this stabilization time, the test articles are initially covered by an ice accretion protection shield. After one minute of cloud stabilization the shield is quickly pulled out of the test section to start the ice accretion process at steady state cloud conditions.

## 3. Numerical setup

A detailed description of the ONERA icing tool IGLOO2D is given in [45]. IGLOO2D is mainly composed of five components (see Fig. 16):

- The MESH2D grid generation tool is dedicated to the building of structured, unstructured and hybrid grids.
- The AERO2D aerodynamic flow solver computes the aerodynamic field (air pressure, velocity and temperature, recovery temperature, heat transfer coefficient and local water vapor mass fraction). It can be obtained by the resolution of the Reynolds-averaged Navier-Stokes equations or by the coupling between the solution of the inviscid equations (potential flow theory or Euler equations) for the external flow field and the resolution of the boundary layer equations (Prandtl equations). In this study AERO2D has been set to inviscid mode with the resolution of the Euler equations in combination with the Prandtl boundary layer equations.

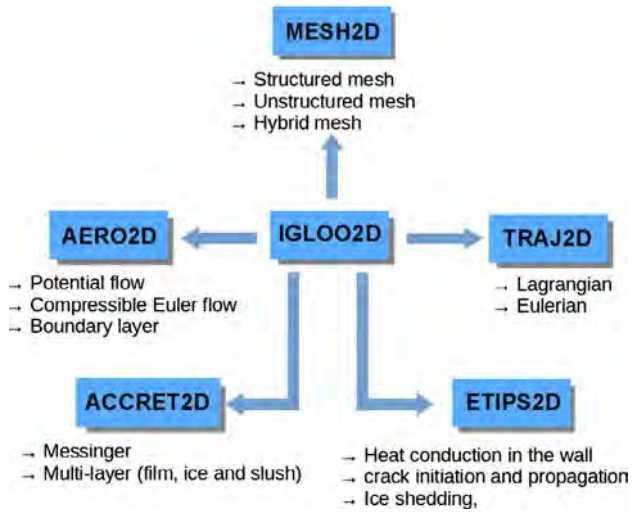


**Fig. 16.** IGLOO2D organization chart.

- The TRAJ2D trajectory solver is dedicated to the computation of the particulate flowfield (crystals and droplets). Two solvers respectively based on a Lagrangian (TRAJL2D) and an Eulerian (TRAJE2D) description are available.
- The ACCRET2D ice accretion solver computes ice accretion from the outputs provided by the aerodynamic and the dispersed two-phase flow solvers.
- The ETIPS2D solver is dedicated to the electro-thermal ice protection system. Ice shedding as well as crack initiation and propagation in the ice core are taken into account. This solver has not been used in the present study.

### 3.1. Accretion model

#### 3.1.1. Main assumptions

In [31,35] an extension of the Messinger model [30] was proposed to account for the presence of ice crystals among the impinging particles. Both mass and energy equations have been adapted with the following assumptions:

H1: The liquid water may not locally accumulate and is carried downstream by the air flow.
H2: All the ice crystals stay where they impinge. They cannot be carried downstream by the running liquid water.
H3: The temperature variation inside the ice layer in the normal direction to the wall can be neglected.

The first assumption is least justified and has been made in [31,35] for the sake of simplicity and because it is one of the main hypothesis of the Messinger model for usual icing conditions [30]. However for ice crystal icing conditions, there is experimental evidence [19] that liquid water may be trapped between the accreted ice particles, leading to the formation of spongy ice deposits. To account for this experimental fact, we proposed in [36] to replace hypothesis H1 by the following new hypothesis H1'.

H1': The liquid water may accumulate in the porous ice layer and the higher the ratio IWC/TWC, the higher is the part of the liquid water trapped between the accreted ice particles. Porosity $\Phi$ is defined as:

$$\Phi = \frac{\dot{m}^L_{acc}/\rho_L + \dot{m}_{air}/\rho_a}{\dot{m}^L_{acc}/\rho_L + \dot{m}_{air}/\rho_a + \dot{m}^S_{acc}/\rho_S} \tag{2}$$

where $\dot{m}^L_{acc}$ (resp. $\dot{m}_{air}$) is the mass rate of liquid water (resp. air) which remains trapped inside the porous ice layer and $\dot{m}^S_{acc}$ is the accreted ice mass rate. $\rho_L, \rho_S$ and $\rho_a$ are respectively the densities for liquid water, solid ice and air. If the porous ice layer is not compacted in some manner, the porosity $\Phi$ is about 40% since this is a typical value for close-packed monodispersed spheres. Actually, $\Phi$ is ranged between 26% for a face-centered cubic or a hexagonal close-packed distribution and 66% for a diamond cubic structure.

As in [36], a simplified model is proposed in this paper to predict which part of the liquid water will runback downstream and which part will be trapped locally.

#### 3.1.2. Model formulation

The evolution of the ice block shape during the whole accretion process (whose duration is denoted by $t$) is captured by a time multi-step algorithm where the ice shape is continuously updated from the inputs (aerodynamics, impinging crystal and droplet mass flow rates, geometric evolution of the ice shape) computed at each time step. The duration of the whole accretion process $t$ is divided into $N$ time steps of size $\Delta t$. At each time step, a fractional time step method is applied. The first step is dedicated to the mass and

energy balances. The second one accounts for the erosion effects while the third one deals with the water accumulation and runback phenomena. In each control volume of the ice layer, the following algorithm is applied:

Step 1: The equations of the models are detailed in [35] and are based on the same fundamental principles like in the original Messinger approach [30]. For the sake of clarity and to define the notations, the equations for the mass balance are written hereafter. Only three cases may occur:

- The control volume contains only ice (rime ice conditions):

$$\dot{m}^S_{acc} = \dot{m}_{rbi} + \dot{m}^L_{dep} + \dot{m}^S_{dep} - \dot{m}_{sub} \tag{3}$$

- The control volume contains a water liquid film only (running wet conditions without ice):

$$\dot{m}^L_{Mess} = \dot{m}_{rbi} + \dot{m}^L_{dep} + \dot{m}^S_{dep} - \dot{m}_{ev} \tag{4}$$

- The control volume contains both ice and liquid water (glaze ice conditions):

$$\begin{aligned} \dot{m}^L_{Mess} &= \dot{m}_{rbi} + \dot{m}^L_{dep} - \dot{m}_{ev} - \dot{m}_f \\ \dot{m}^S_{acc} &= \dot{m}^S_{dep} + \dot{m}_f \end{aligned} \tag{5}$$

where $\dot{m}_{rbi}$ is the incoming runback liquid water mass rate, $\dot{m}^L_{dep}$ is the deposited mass rate of liquid water (coming from both impinging liquid droplets and melted ice crystals), $\dot{m}^S_{dep}$ is the deposited mass rate of solid ice (coming from impinging ice crystals), $\dot{m}_{sub}$ is the sublimation mass rate, $\dot{m}_{ev}$ is the evaporation mass rate, $\dot{m}^L_{Mess}$ is the net liquid water mass rate (i.e. the mass rate corresponding to the liquid water which did not evaporate, sublimate or freeze during the corresponding time step), $\dot{m}^S_{acc}$ is the accreted ice mass rate and $\dot{m}_f$ is the algebraic freezing mass rate (negative in case of melting). $\dot{m}^L_{dep}$ and $\dot{m}^S_{dep}$ mass rates are related to the droplet and ice crystal impinging mass rates by the sticking efficiency whose expression is given below.

Step 2: $\dot{m}^L_{Mess}$ and $\dot{m}^S_{acc}$ are updated to take into account the erosion effects according to the model of Eq. (14) described later on.

Step 3: The mass rate $\dot{m}^L_{Mess}$ can be split as follows:

$$\dot{m}^L_{Mess} = \dot{m}^L_{acc} + \dot{m}_{rbo} \tag{6}$$

where $\dot{m}^L_{acc}$ is the mass rate of liquid water which remains trapped inside the porous ice layer and $\dot{m}_{rbo}$ is the mass rate of running back liquid water. Expressions for $\dot{m}_{rbo}$ and $\dot{m}^L_{acc}$ will be given hereafter.

### 3.1.3. Model for the sticking efficiency coefficient

This part is dedicated to the computation of $\dot{m}^L_{dep}$ and $\dot{m}^S_{dep}$ from the impinging droplet and ice crystal mass rates (respectively $\dot{m}_{imp,d}$ and $\dot{m}_{imp,c}$):

$$\begin{aligned} \dot{m}^L_{dep} &= \dot{m}_{imp,d} + \epsilon_s \eta_m \dot{m}_{imp,c} \\ \dot{m}^S_{dep} &= \epsilon_s (1 - \eta_m) \dot{m}_{imp,c} \end{aligned} \tag{7}$$

where $\epsilon_s$ is the ice crystal sticking efficiency. $\epsilon_s$ correlates with the difference of impinging and rebounding particles. In this paper, ice crystals are not melted so that $\eta_m = 0$. The model proposed for $\epsilon_s$ is:

$$\epsilon_s = F(m_{r,stick}) \tag{8}$$

where $m_{r,stick}$ is the ratio of liquid to total water content at the wall necessary for the ice crystals to stick to the wall. Two different models for $m_{r,stick}$ are proposed for the two ice crystal icing regimes. For the glaciated regime where the liquid water comes from the melted part of the initially glaciated ice crystals (Currie et al. [18]), the following model for $m_{r,stick}$ is used:

$$m^{glaciated}_{r,stick} = \eta_m \tag{9}$$

For the mixed phase regime (like in the present study) with a mix of ice crystals and droplets, $m_{r,stick}$ is modelled as:

$$m^{mixed}_{r,stick} = K_d \cdot f_l \tag{10}$$

where $f_l$ is the total liquid fraction at the wall defined as:

$$f_l = \frac{\dot{m}^L_{acc} + \dot{m}_{rbo}}{\dot{m}^L_{acc} + \dot{m}_{rbo} + \dot{m}^S_{acc}} = \frac{\dot{m}^L_{Mess}}{\dot{m}^L_{Mess} + \dot{m}^S_{acc}} \tag{11}$$

$K_d$ is an adjustable parameter. It has been calibrated in [36] by comparing the computed ice shapes with the experimental ones from the databases of Al-Khalil et al. [22] and Currie et al. [16]. However, the models for $m^{mixed}_{r,stick}$ are slightly different between Eq. (10) and Eq. (49) from [36]. Notably in [36], the function $F$ is the identity function and the ratio of liquid water to total water content at the wall is given by the ratio $LWC/TWC$ instead of $f_l$. The value for $K_d$ calibrated in [36] has been used as a first guess in this study and it has been confirmed to $K_d = 0.3$ after several guesses based on the computations proposed in this paper. If we come back on the model of Eq. (10), the ratio of liquid water to total water content at the wall is given by $f_l$ which is more relevant than the classical $LWC/TWC$ for mixed phase conditions used in [36]. Indeed, for pure ice crystals where $LWC/TWC = 0$, the only available liquid water which allows ice crystals to stick to the wall comes from the runback film which is itself defined by $f_l > 0$.

The function $F$ (Eq. (8)) is set from the Currie et al. experiments [18] where it is shown that for a crowned cylinder and for partially melted ice crystals, the net stagnation point sticking efficiency (i.e. combining both the ice crystal sticking efficiency and the losses due to erosion) is a function of $m_{r,stick} = \eta_m$ (Fig. 17(a)). In the present work (see Eq. (14)), it is supposed that the erosion rate is proportional to the tangential kinetic energy of the impinging ice crystals so that the erosion rate is very low near the stagnation point where the velocity of the impinging particles is normal to the wall. This is why it is acceptable to use Currie's data [18] to fit our model for the $F$ function. Given the experimental data for $0 < m_{r,stick} < 0.2$ (Fig. 17(a)) and given that $F$ is expected to be a smooth increasing function which tends to 1 when $m_{r,stick} \to 1$, the following polynomial expression has been chosen for $F$:

$$F(m_{r,stick}) = (K^{\#} - 2) m^3_{r,stick} + (3 - 2K^{\#}) m^2_{r,stick} + K^{\#} m_{r,stick} \tag{12}$$

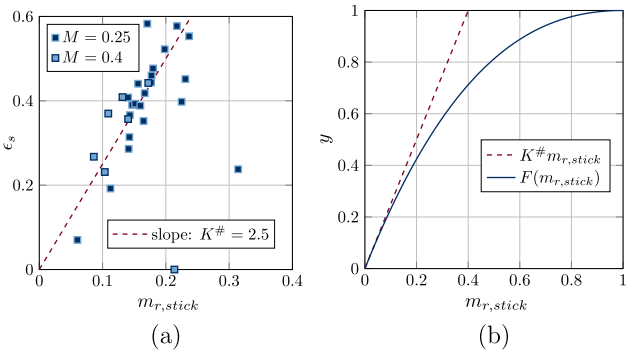


**Fig. 17.** (a): $\epsilon_s$ vs. $m_{r,stick}$ (from Currie et al. [18]). Here $m_{r,stick} = m^{glaciated}_{r,stick} = \eta_m$. The dashed line stands for $\epsilon_s = K^{\#} \cdot m_{r,stick}$ with $K^{\#} = 2.5$ (see [18]). (b): $F(m_{r,stick})$ (see Eq. (12)). The dashed line is the tangent line to the function $F$ for $m_{r,stick} = 0$.

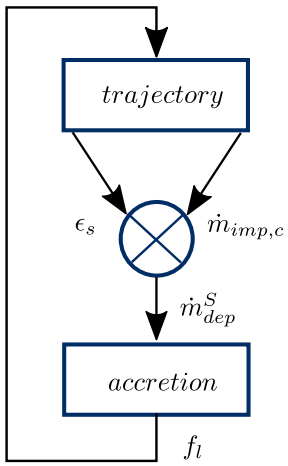


**Fig. 18.** Coupling between the trajectory and accretion solvers in the icing suite IGLOO2D [45].

The function $F$ is represented in Fig. 17(b). Given [18], the coefficient $K^{\#}$ is chosen to be 2.5.

Eq. (8) shows an explicit coupling between the trajectory solver (where $\epsilon_s$ is computed with $f_l$ as an input, see Eq. (8)) and the accretion solver (where $f_l$ is computed as an output). This coupling is summarized in Fig. 18.

### 3.1.4. Erosion model

The erosion mass rate $\dot{m}_{er}$ is defined as:

$$\dot{m}_{er} = \min\left[\dot{m}^S_{acc} + \dot{m}^L_{Mess}, \min(1, \epsilon_{er})\dot{m}_{imp,c}\right] \tag{13}$$

where the erosion efficiency $\epsilon_{er}$ is given by:

$$\epsilon_{er} = E \cdot \underbrace{\left(\frac{V^t_{imp,c}}{V_0}\right)^2}_{①} \cdot \underbrace{\frac{y_{l0}}{y_{l0} - \min(y_l, y_{l0})}}_{②} \cdot \underbrace{\left[1 + (l_0\kappa)^2\right]}_{③} \tag{14}$$

$y_l$ is the wall liquid mass fraction defined by:

$$y_l = \frac{\dot{m}^L_{acc}}{\dot{m}^L_{acc} + \dot{m}^S_{acc}} \tag{15}$$

The different terms (①, ② and ③) are detailed in [36]. Only the term ② is different from [36]. The expression of term ② is based on a phenomenological approach. By construction, term ② tends to infinity when the wall liquid mass fraction $y_l$ gets close to a critical value denoted by $y_{l0}$. This is directly related to experimental facts: in ice crystal icing conditions, an ice layer cannot appear if the liquid mass fraction is too high (see Fig. 1). For clarity reasons, some terms from Eq. (14) must be defined:

- $V^t_{imp,c}$ denotes the mean tangential velocity of the impinging ice crystals.
- $\kappa$ is the local curvature of the wall (or of the ice layer surface) defined by:

$$\kappa(s,t) = \left|\frac{x'(s,t)\cdot y''(s,t) - y'(s,t)\cdot x''(s,t)}{\left[x'^2(s,t) + y'^2(s,t)\right]^{3/2}}\right| \tag{16}$$

  where the derivative $\cdot'$ means $\frac{d}{ds}\cdot$ and $(x(s,t); y(s,t))$ defines the Cartesian coordinates of the point on the clean profile or the ice layer upper surface located at the curvilinear abscissa $s$ at time $t$. The higher the local curvature, the higher the erosion rate. This term accounts for the smoothing effect of erosion which tends to remove surface irregularities for which typical length scale is smaller than a critical value corresponding to $l_0$ in the present model.
- $E, y_{l0}$ and $l_0$ are empirical constants calibrated from the experiments of Currie et al. [18] related to the glaciated regime. A sensitivity analysis of the computed ice shapes with respect to the magnitudes of $E, y_{l0}$ and $l_0$ is presented in [46]. In the present study and after several guesses for the parameters $E, y_{l0}$ and $l_0$ to get the best possible agreement between model predictions of ice accretion shapes and experimental results, the same set of parameters as in [46] has been chosen:

$$\begin{aligned} E &= 0.3 \\ y_{l0} &= 0.6 \\ l_0 &= 0.015 \cdot c \end{aligned} \tag{17}$$

  where $c$ is the chord of the profile.

### 3.1.5. Runback model

The water mass flow rate $\dot{m}^L_{Mess}$ (Eq. (6)) is split between $\dot{m}^L_{acc}$ and $\dot{m}_{rbo}$ as follows:

$$\begin{aligned} \dot{m}^L_{acc} &= \min\left[G(\Phi)\cdot(1-\xi_l^2)\cdot\dot{m}^S_{acc};\quad \dot{m}^L_{Mess}\right] \\ \dot{m}_{rbo} &= \dot{m}^L_{Mess} - \dot{m}^L_{acc} \end{aligned} \tag{18}$$

where $\xi_l$ is defined as:

$$\xi_l = \frac{\dot{m}^L_{dep}}{\dot{m}^L_{dep} + \dot{m}^S_{dep}} \tag{19}$$

and $G$ is an increasing function of $\Phi$, the porosity of the accreted ice ($0 < \Phi < 1$). In the absence of experimental data dedicated to the modelling of $\Phi$, the function $G$ is set to one ($G = 1$) in this study. Note that in the case of pure liquid water droplets, $\xi_l = 1$ and the model of Eq. (18) gives $\dot{m}^L_{acc} = 0$ which proves that the model of Eq. (18) is compatible with the hypothesis H1 of the classical Messinger model [30] for the supercooled droplet icing regime.

### 3.1.6. Computational setup

A C-grid topology (see Fig. 19 for the NACA 0012 profile) has been used in this study with a farfield boundary condition at the outer boundary. Space (grid) and time (influence of the number of time steps $N$, see Section 3.1.2) convergence studies have been carried out. Two grids have been used (Fig. 20(a)). The coarse grid (resp. the fine grid) is a structured (resp. unstructured) grid made of quadrangles (resp. triangles) with 129 (resp. 1022) nodes on the profile and a total of 4000 (resp. 66,500) cells in the computational domain. The coarse grid is refined near the leading edge.

Fig. 20(b) shows ice accretion after 120 s of icing at $TWC = 12$ g/m$^3$ and $m_r = 0.2$ both for the coarse and fine grids. The ice shapes are similar for the two grids. Therefore, the coarse

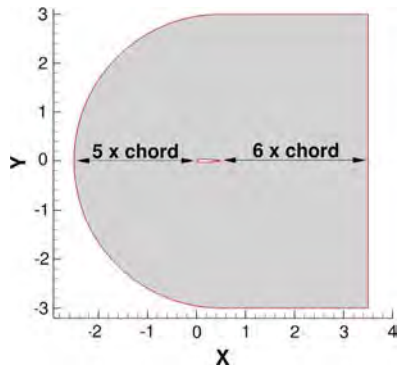


**Fig. 19.** NACA 0012: C-grid topology. Farfield boundary conditions are applied at the outer boundary at distances from 5 to 6 chord lengths from the test article.

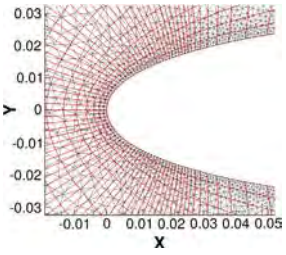


a) red: structured coarse grid (quadrangles with 129 nodes on the profile and 4000 cells in the computational domain). Black: unstructured fine grid (triangles with 1022 nodes on the profile and 66500 cells in the computational domain).

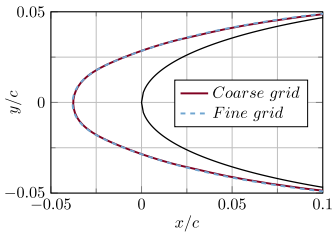


b) Ice accretion after 120 seconds of icing at $TWC = 12\ g/m^3$ and $m_r = 0.2$. $N = 10$.

**Fig. 20.** NACA 0012: Mesh convergence.

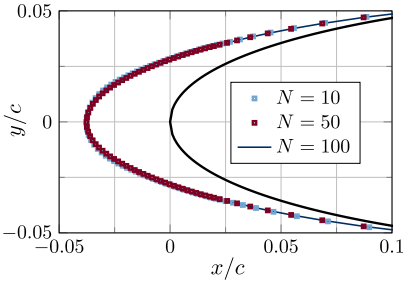


**Fig. 21.** NACA 0012: Time convergence and influence of the number of time steps *N*. The structured coarse grid is used.

grid has been used in the course of this study. Concerning the time convergence, the influence of the parameter *N* (see Section 3.1.2) is exemplified in Fig. 21. The ice shapes are similar for $N = 10, N = 50$ and $N = 100$. Therefore, $N = 10$ has been set for all simulations.

## 4. Ice accretion studies

### *4.1. Ice particle sticking*

As explained in the previous chapter, ice accretion at mixed phase conditions is governed by the mass of ice particles and liquid phase that effectively sticks to the test body. An appropriate parameter to quantify the amount of sticking ice and water mass is the stagnation point accretion efficiency $\alpha_0$. It corresponds to the amount of water and ice that gets locally incorporated to the ice accretion at the leading edge position, compared to the total mass which locally impinges. A mathematical formulation of the accretion efficiency is given by Eq. (20).

$$\alpha_0 = \frac{\dot{t}_l \cdot \rho_{acc}}{\beta_0 \cdot TWC \cdot U_\infty} \tag{20}$$

Eq. (20) includes the accretion growth rate $\dot{t}_l$, which corresponds to the change of accretion thickness in time, see Fig. 22. The ice density $\rho_{acc}$ considers the ice accretion to be a compound of solid ice and liquid water. The composition is assumed to be proportional to the melting ratio of the icing cloud. The accretion efficiency further

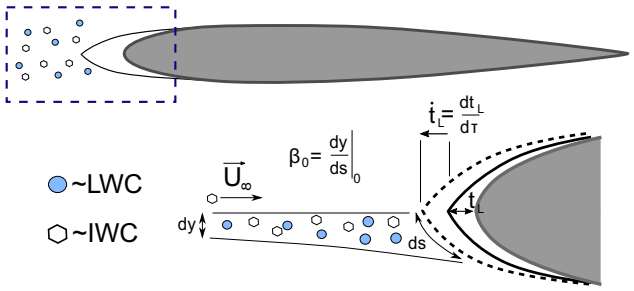


**Fig. 22.** Mixed phase ice accretion: Collecting efficiency $\beta_0$ and accretion growth rate $\dot{t}_L$.

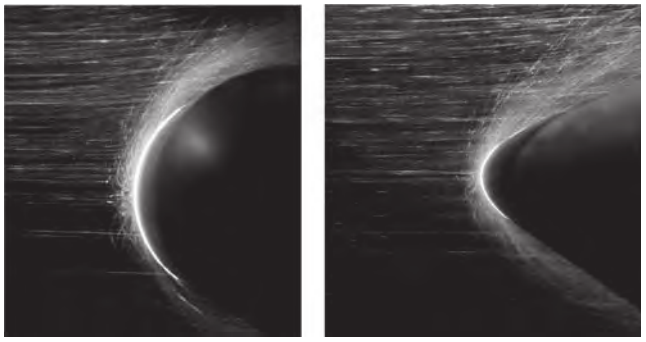

(a) cylinder model (b) NACA 0012 airfoil

**Fig. 23.** Ice particle impact at glaciated icing conditions ($U_\infty = 40$ m/s, $MMD = 80$ µm), particle trajectories highlighted by laser sheet illumination.

requires the stagnation point collection efficiency $\beta_0$. As indicated in Fig. 22, $\beta_0$ quantifies the amount of ice particles and droplets hitting the surfaces in the stagnation point compared to the particle flow approaching the test article. In contrast to the accretion growth rate $\dot{t}_l$, the accretion efficiency allows to quantify icing severity independently of the total amount of impinging ice and water mass because $\alpha_0$ is a dimensionless parameter normalized by the total water content *TWC*.

Fig. 23 shows fully glaciated ice particles bouncing off the test article surface. The impinging and rebounding particles have been illuminated by the laser light sheet. The camera exposure time has been set to 1/100 s, which is an appropriate time interval to visualize ice particle trajectories. The trajectories indicate a rather ballistic particle flow behaviour due to high particle inertia. Both images of Fig. 23 are taken at fully glaciated conditions. Except from the stagnation point area, the ice particles rebound off the surface and do not re-impact on the test model.

Fig. 24 shows a contour plot of pressure distribution around the cylinder model based on IGLOO2D simulations. The image includes stream traces to visualize the aerodynamic flow field. Further, particle trajectories for ice crystals of 80 µm diameter are superimposed and highlighted in blue color. As AERO2D has been set to inviscid mode, flow separation off the cylinder surface is not captured in the simulation. Comparisons to viscous flow computations have proved that the flowfield downstream of the cylinder does not affect the ice particle flow upstream of the test article. It is shown in [47] that the front-side impingement efficiency of particles on a cylinder has the same dependency on the Stokes number for all Reynolds numbers. The particle follow up behavior of the experiments could be reproduced in the simulations. Due to high particle inertia, the trajectories exhibit little curvature, producing high collection efficiencies in the stagnation point region.

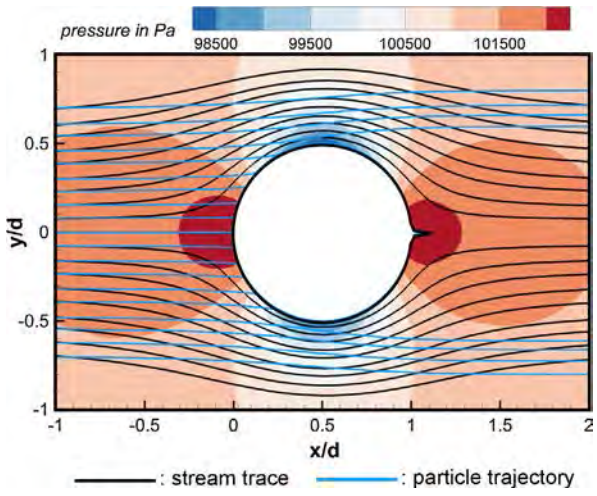


**Fig. 24.** Flowfield around the cylinder model based on IGLOO2D simulations, $U_\infty = 40$ m/s, pressure distribution, stream traces and particle trajectories for $d_p = 80$ μm. The little spike in the back of the cylinder is a numerical trick to build a structured grid around the cylinder with no consequences on the aerodynamic flowfield computation.

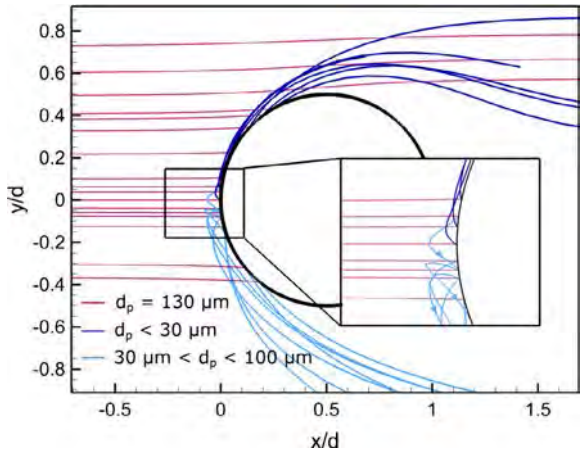


**Fig. 25.** Ice particle impact on cylinder model based on IGLOO2D simulations ($U_\infty = 40$ m/s and $MMD = 130$ μm), secondary particle trajectories.

Fig. 25 shows trajectories of ice particle fragments rebounding off the cylinder surface. The particle initial diameter has been set to $MMD = 130$ μm to highlight the difference between large and small fragment rebound behavior. The dark blue lines in the upper half of the image represent particle fragments of less than 30 μm diameter. Trajectories of ice particle fragments of about 80–90 μm diameter are highlighted by bright blue lines. These large ice particle fragments are deflected further into the flow field compared to the small fragments due to higher inertia. Except for a very narrowed region around the stagnation point, no ice particles re-impact on the cylinder surface. It can be concluded that the contribution of secondary particle impact on the overall ice accretion process is rather limited. Especially in the outer regions of the ice accretion secondary impact of low momentum ice particle fragments is rather unlikely. To save computational time it has been decided to deactivate the option of secondary particle tracking in IGLOO2D for the studies presented in this paper. Fig. 26 shows the negligible influence of secondary particle impact on the final accretion shape based on IGLOO2D simulations.

As described above, the stagnation point accretion efficiency $\alpha_0$ is an appropriate parameter to quantify icing severity. Fig. 27 includes plots of $\alpha_0$ against melting ratio for the cylinder model based on wind tunnel experiments. In addition, results from NRC studies described in the introduction are included [18]. It has to be stressed that the NRC studies are performed at Mach numbers of M = 0.25 and M = 0.4. while in the present study M is 0.12. Moreover, the NRC tests have been conducted with smaller particles at wet bulb temperatures above the freezing point which typically cause spongy ice accretions of low solidity. Further more, it has to be pointed out that melting simulations of Currie [48] indicate that the $m_r$ values yielded from hot-wire LWC measurements of partially melted particles are possibly only half of the actual value. In this case, the agreement between NRC and TUBS results in Fig. 27 would be much better. NRC tests at wet bulb temperatures below freezing have yielded accretion efficiencies in the range of 0.06–0.23 [17]. High values of $\alpha_0$ could be correlated with an increase of melting ratio and total water content as well as decreasing temperature. The last point is in contrast to TUBS observations according to Fig. 27 and might be addressed to differences in Mach number and particle size distribution.

The accretion efficiencies listed in Fig. 27 are averaged over 120 s. Changes of the accretion tip angle are taken into account in the collection efficiency. $\beta_0$ is calculated based on the assumption of straight horizontal trajectories of impinging particles.

In addition to the cylinder model, Fig. 28(a) shows plots of accretion efficiency for the NACA 0012 airfoil. The plots are very similar for the cylinder and the NACA 0012 model. Highest icing severity is given for a melting ratio of 0.28. At 0 °C wet bulb temperature, the right end of the icing plateau is above a melting ratio of 0.6. For $T_\infty = -5$ °C and $T_\infty = -15$ °C no right end of the regime is existent as the icing process changes to supercooled droplet icing at $m_r = 1$.

A strong temperature dependency of $\alpha_0$ can be observed for both test articles. At 0 °C better sticking is given for moderate melting ratios up to $m_r$ = 0.4. For higher melting ratios better sticking is given at −5 °C. It has to be pointed out that mixed phase tests at −15 °C have yielded significantly lower accretion efficiencies compared to tests at 0 °C and −5 °C. Comparing both test articles, the obtained accretion efficiencies are in good agreement. For melting ratios in the range of 0.1–0.3, slightly higher values can be observed for the cylinder model.

In Section 2.4 it has been reported that the test articles have been applied with black aluminum tape to better detect ice accretions in side view video sequences. It turned out that the aluminum tape has an influence on the accretion process even if it covers only one half of the test article. Because of higher roughness of the aluminum tape compared to the blank surfaces of the aluminum center bodies of both test articles, ice accretion is intensified. In the course of this study, two test campaigns have been conducted. Fig. 28(b) shows the influence of the aluminum tape on accretion efficiency at $T_\infty = -5$ °C. The dark dashed line represents measurements from the first test campaign where no aluminum tape had been applied. In the following discussion, the results of the first campaigns are not included because the evaluation of the second campaign results is much more precise and reliable. Anyway, the influence of surface roughness has to be kept in mind for data interpretation.

Fig. 29 shows plots of accretion efficiency versus melting ratio based on IGLOO2D computations. The simulations yield accretion efficiencies of more than 0.5 which is higher than observed in the experiments. The temperature effect observed in the experiments could only partially be reproduced in the simulations. Only at low melting ratios highest icing severity is given at 0 °C while for higher melting ratios enhanced sticking is observed at −5 °C. However, the strong decrease in accretion efficiency for $T_\infty = -15$ °C is not reproduced in the simulations very precisely. As explained later in the paper, particle sticking at low temperatures seems to

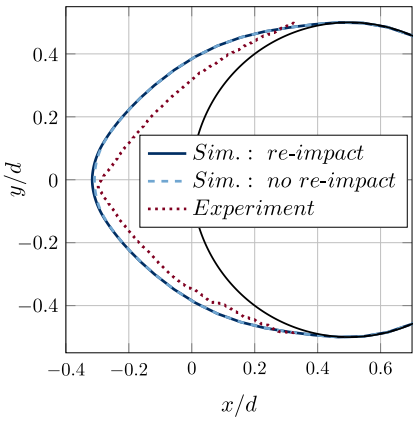


**Fig. 26.** Influence of secondary particle impact, $T_\infty = 0\,^\circ$C,$m_r = 0.12$, $TWC = 12$ g/m$^3$.

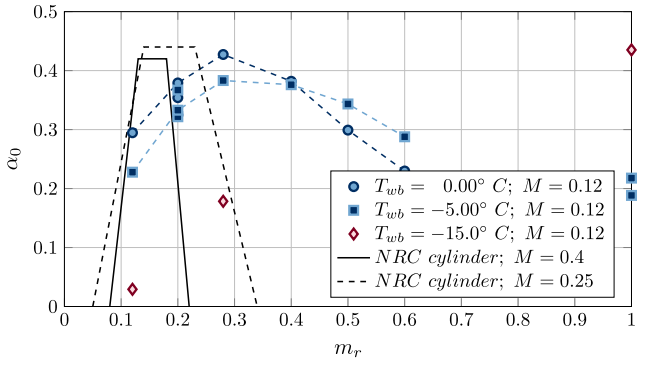


**Fig. 27.** Cylinder: Accretion efficiencies based on outcomes of the second test campaign, NRC results included according to [18].

be overestimated in the current version of the model. Further more, enhanced erosion might take place at low temperatures due to dry and more brittle accretion structures.

### *4.2. Temperature influence on ice accretion growth*

The experimental results have indicated a strong effect of temperature on icing severity for mixed phase clouds below freezing. This temperature effect could be caused by multiple factors, where two of the most important are discussed below.

First, enhanced convective cooling at lower temperatures promotes a greater mass of liquid water to freeze on the accretion surface. The amount of solid ice incorporated in the accretion increases, resulting in strong accretion compounds at low temperatures. This behavior can be observed in Fig. 30 where the influence of temperature on the freezing mass rate $\dot{m}_f$ is shown based on IGLOO2D simulations. *TWC* and $m_r$ are set to 12 g/m$^3$ and 0.28. $\dot{m}^L_{dep}$ and $\dot{m}^S_{dep}$ quantify the amounts of liquid droplets and solid ice particles that deposit on the accretion layer. $\dot{m}_f$ represents the freezing rate of depositing liquid, which is highest at the lowest temperature of $-15\,^\circ$C. At $0\,^\circ$C,$\dot{m}_f$ is negative, which means that some impinging ice crystals melt because of kinetic energy dissipation. Therefore, temperature influences accretion efficiency from an energetic perspective as cooling forces liquid water to freeze.

Secondly, the temperature has an indirect influence on $\epsilon_s$, the ice crystal sticking efficiency. Enhanced freezing at lower temperatures allows less liquid water to accumulate inside the accretion layer. The sticking efficiency $\epsilon_s$ is coupled to the liquid mass flux $\dot{m}^L_{Mess}$ (Eq. (6)) by the total liquid fraction $f_l$, see Eqs. (8) and (11).

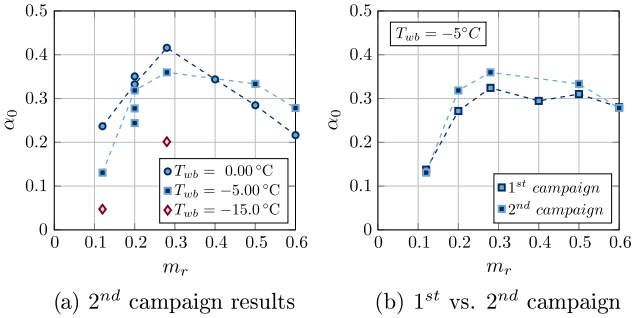


**Fig. 28.** NACA 0012: Accretion efficiencies based on outcomes of the first and second test campaign.

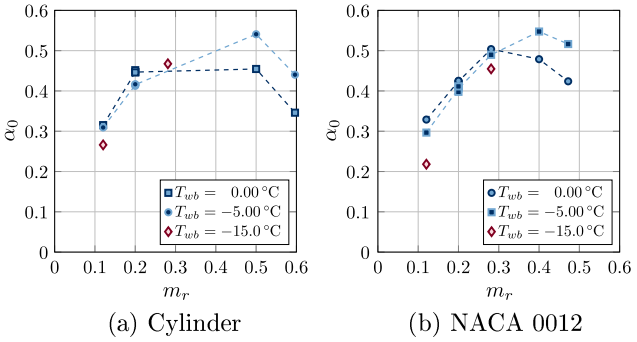


**Fig. 29.** Accretion efficiencies based on IGLOO2D simulations.

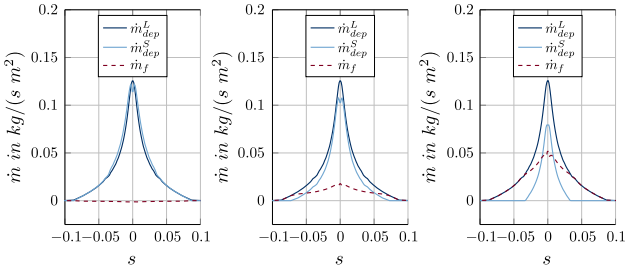


**Fig. 30.** NACA 0012: Freezing mass rate $\dot{m}_f$ depending on ambient static temperature, IGLOO2D simulations for $TWC = 12$ g/m$^3$ and $m_r = 0.28$.

Higher freezing rates cause $\dot{m}^L_{Mess}$ and $f_l$ to decrease, resulting in less ice particle deposition $\dot{m}^S_{dep}$. This dependency is illustrated Fig. 31 in which $\dot{m}_{imp,c}$, $\dot{m}^S_{dep}$ and $f_l$ are plotted for various temperatures but same cloud conditions. As in Fig. 30, *TWC* and $m_r$ are respectively set to 12 g/m$^3$ and 0.28. So, the impinging mass flux of solid ice particles $\dot{m}_{imp,c}$ is equal for all plots in Fig. 31. In contrast, $f_l$ decreases with temperature due to enhanced freezing as described above. It follows that also $\dot{m}^S_{dep}$ decreases. Less particles effectively stick to the accretion surface at lower temperatures. It can be summarized that temperature significantly influences the accretion process as it affects the solidification of the accretion structure and so its sensitivity for particle sticking. Also, enhanced erosion of dry and brittle accretion structures at low temperatures is plausible. Erosion of brittle deposits correlates with the normal particle impact velocity which is not respected in the current version of IGLOO2D.

The test models of the experiments are manufactured from aluminum, which features a rather high thermal conductivity of

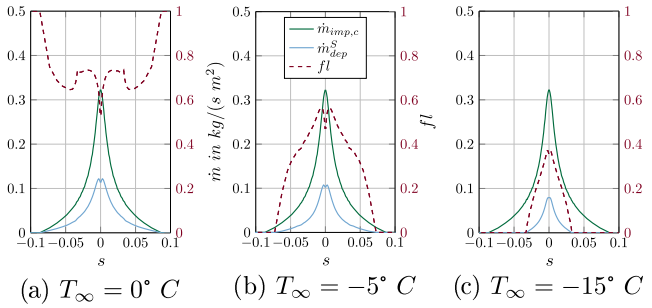


**Fig. 31.** NACA 0012: Ice particle deposition depending on ambient static temperature, IGLOO2D simulations for $TWC = 12\ \mathrm{g/m^3}$ and $m_r = 0.28$.

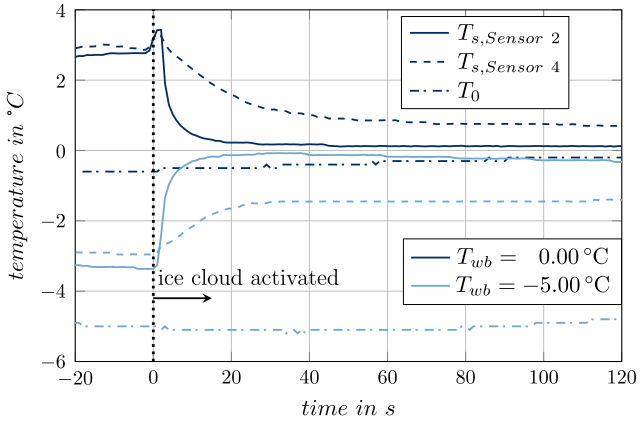


**Fig. 32.** Surface temperatures of the NACA 0012 airfoil during the ice accretion process depending on ambient temperature, $TWC = 12\ \mathrm{g/m^3}$ and $m_r = 0.28$.

120 W/mK. Thus, heat conduction inside the test article can be expected to affect the ice accretion process. Fig. 32 shows plots of surface temperature of the NACA 0012 airfoil during the ice accretion procedure at $T_\infty = 0\,°C$ and $T_\infty = -5\,°C$. The solid lines represent *sensor 15*, which is installed at the tip of the leading edge of the NACA 0012 airfoil. In addition, the dashed lines represent *sensor 4* which is installed 50 mm downstream. Fig. 33 illustrates the corresponding sensor positions. Ambient air temperatures are indicated by dashed dotted lines. Figs. 34 and 35 show images of the NACA 0012 airfoil from top view perspective in which the sensor positions are marked. The images result from the first test campaign where the black aluminum tape was not applied. One can observe significant differences of the accretion structure for temperatures of 0 °C and −5 °C from the top view images. At $T_\infty = 0\,°C$ the accretion features a slushy structure, slices of ice are continuously dragged downstream by shear stresses of the airflow. In contrast, at $T_\infty = -5\,°C$ the region downstream of the actual ice accretion is covered by small roughness elements. These elements can be expected to mostly originate from liquid film freezing and subsequent droplet- and eventual ice particle accretion. In both images it can be observed that after 120 s of ice accretion *sensor 15* at leading edge is fully covered by ice while *sensor 4* is not.

The temperature plots of Fig. 32 show that it takes about 20 s to reach freezing temperature at leading edge position for both air

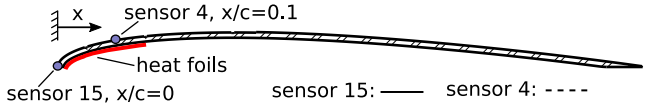


**Fig. 33.** Temperature sensor positions.

temperatures, 0 °C and −5 °C. The initial sensor temperatures deviate from air temperature because the airfoil is covered by the ice accretion protection shield before it is exposed to the stable icing cloud. During this stabilisation time, convective cooling is limited and warm air from inside the test article slightly heats the composite. When the protection shield is removed, the airfoil surface is cooled by ice particle impact and potential melting at $T_\infty = 0\,°C$. The temperature at the stagnation point is subsequently stable at 0 °C. A temperature deviation of about +0.1 °C from the freezing point can be attributed to the sensor measurement accuracy of ±0.15 °C. When the leading edge surface temperature is stable at 0 °C, the normal heat flux from the inner surface has been determined to be 0.31 $\mathrm{W/m^2}$ based on temperature measurements. This heat flux is far to low to cause significant melting of ice accretion on the ice-substrate interface. It has to be pointed out that ice accretion takes place several seconds after the airfoil is exposed to the cloud, before the surface temperature has reached the freezing point.

At $T_\infty = -5\,°C$ the surface temperature increases when the ice flow effectively starts ($t = 0s$). The supercooled liquid phase partially freezes and emits latent heat to the airfoil surface. Based on the temperature distribution indicated by the $Pt_{1000}$ sensors it can be assumed that heat conduction inside the airfoil (in chordwise direction towards the rear body) compensates latent heat of 7% of the impinging droplet mass. As soon as an ice accretion layer has developed, the influence of heat conduction inside the airfoil on droplet freezing diminishes due to insulation effects of the icing layer itself. Anyway, it has to be pointed out that convective cooling of the airfoil rear part causes a drop of surface temperature in the stagnation point due to internal heat conduction (notice a temperature decrease after about 50 s of icing). It has to be mentioned that in case of the cylinder model, the front shell has a very uniform temperature distribution during the ice accretion process. The cylinder surface also reaches the freezing point after about 20 s of icing and can be considered as adiabatic in the following. At −15 °C the surface temperature of the cylinder and the NACA 0012 airfoil rises as the mixed phase cloud is effectively launched. In contrast to $T_\infty = -5\,°C$, the surface temperature never reaches the freezing point. It can be summarized that in the present study, where no internal heating has been applied to the test articles, thermal conductivity of the test article has no first order effect on the icing process.

From a numerical point of view, as illustrated in Fig. 16, IGLOO2D calls the module ETIPS2D to model heat conduction inside the test body. ETIPS2D has been implemented to IGLOO2D in the very recent past and is not applied for the simulations presented in this paper. Thus, the test bodies are considered as adiabatic walls. This hypothesis is not restrictive since the ice accretion behaves like an outer insulating layer to the test article. Moreover, for $T_\infty = 0\,°C$ (glaze ice) no temperature gradient is present among the ice accretion. It is a two phase mixture which is neither affected by convective or evaporative cooling at $T_{wb} = 0\,°C$ nor by heat conduction from the substrate.

The top view images in Figs. 34 and 35 show significant differences in the ice accretion structure downstream of the stagnation point region. Fig. 36 stresses that also the primary accretion shape around the leading edge is strongly dependent on ambient temperature. Fig. 36 shows side view ice accretion images yielded from icing experiments at different temperatures but same ice cloud conditions. A constant TWC of $12\ \mathrm{g/m^3}$ has been set at $m_r = 0.28$ which corresponds to optimum icing conditions according to Fig. 28. The left image of Fig. 36 shows ice accretion after 60 and 120 s at a static air temperature of 0 °C. The accretion is characterized by a rather clean surface that smoothly merges with the airfoil. Ice accretion shedding occurred after 170 s of icing. Before,

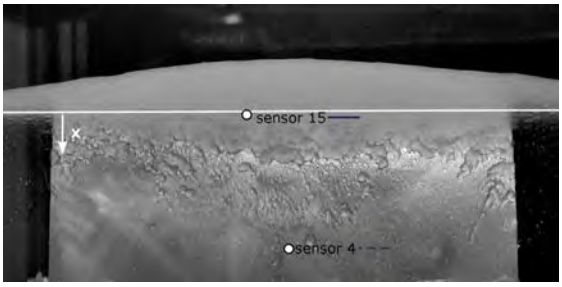


**Fig. 34.** Top view: Ice accretion after 120 s, $TWC = 12\ \mathrm{g/m^3}, m_r = 0.28, T_\infty = 0\ ^\circ\mathrm{C}$.

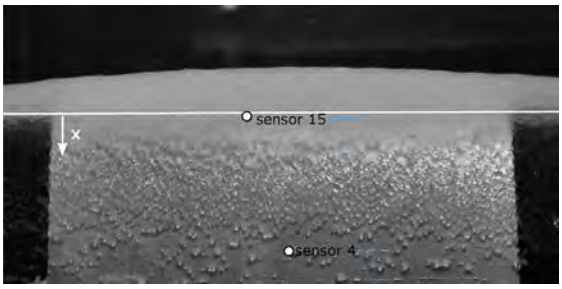


**Fig. 35.** Top view: Ice accretion after 120 s, $TWC = 12\ \mathrm{g/m^3}, m_r = 0.28, T_\infty = -5\ ^\circ\mathrm{C}$.

the ice accretion slightly drooped due to gravity effects and then instantly shed due to low adhesion. The steady surface temperature of 0 °C in Fig. 32 indicates that the accretion is a composition of mixed phase ice which is pressed against the airfoil leading edge by the surrounding air flow but does not develop an adhesive connection due to the presence of liquid water. For $T_\infty = -5\ ^\circ\mathrm{C}$ convective cooling is sufficient to form an adhesive bridge between ice accretion and airfoil surface. The accretion continuously grows and does not tend to shed. Compared to Fig. 36(a) at 0 °C the accretion surface is very rough. No smooth transition to the airfoil surface can be observed as the downstream region of the accretion is characterized by film freezing and the formation of roughness elements. At −15 °C, see Fig. 36(c) the ice accretion features a very sharp wedge. The test run was stopped after 120 s of icing. Based on growth observations it is expected that the accretion continuously grows with a decreasing accretion angle.

Fig. 37 shows comparisons of ice accretion shapes after 120 s of icing for the experiments and simulations according to the icing conditions of Fig. 36. At 0 °C and −5 °C, the agreement between the experimental and numerical results is rather good. The sharp wedge ice shape is not accurately captured by the model, however. In the present study the flow velocity is $U_\infty = 40$ m/s while the erosion model (Eq. (14)) has been calibrated using NRC experimental data obtained at $U_\infty = 85$ m/s with a different particle size distribution. Assuming the model to be valid at the different conditions of this study, it follows that erosion has no significant effect on accretion shaping in the present study because the simulations yield rather bulky accretion geometries compared to the experiments. On the other hand it follows, that other mechanisms than erosion, which are not respected in the current version of IGLOO2D, have to influence accretion shaping to explain the discrepancies between simulation and experiment. This aspect is restated later in the text. For the lowest temperature of −15 °C, the ice shape is widely overestimated near the leading edge. The sticking efficiency $\epsilon_s$ (Eq. (8)) is overestimated even after temperature effects are taken into account as discussed in Section 4.2. Near the stagnation point (see Fig. 31) total liquid fractions of $f_l = 0.36$ and $f_l = 0.53$ are determined for $T_\infty = -15\ ^\circ\mathrm{C}$ and $T_\infty = 0\ ^\circ\mathrm{C}$, yielding sticking efficiencies of $\epsilon_s = 0.25$ and $\epsilon_s = 0.35$. So, at $T_\infty = 0\ ^\circ\mathrm{C}$ the sticking efficiency is 1.4 times higher than at $T_\infty = -15\ ^\circ\mathrm{C}$. On the other hand, the freezing mass rates $\dot{m}_f$ are $-1.4\ \mathrm{g/m^2\ s}$ and $52\ \mathrm{g/m^2\ s}$ for $T_\infty = 0\ ^\circ\mathrm{C}$ and $T_\infty = -15\ ^\circ\mathrm{C}$ according to Fig. 30. Thus, the large (possibly overestimated) freezing mass rate at $T_\infty = -15\ ^\circ\mathrm{C}$ is not counterbalanced by reduced sticking or enhanced erosion.

### 4.3. Influence of the ice cloud melting ratio on the accretion process

In the previous section the influence of ambient temperature on ice accretion growth has been discussed. In this section the focus is set on the influence of ice cloud composition.

Fig. 38 shows side view images of ice accretion for the same total water content and temperatures as previously presented in Fig. 36. The melting ratio has been lowered from 0.28 to 0.12. In contrast to the previous results, no accretion shedding occurred at ambient temperatures of 0 °C, see Fig. 38(a). For ambient temperatures of −5 °C, icing severity is significantly lower at $m_r = 0.12$ compared to $m_r = 0.28$, see Fig. 38(b). The accretion has a very low volume and a sharp accretion angle, similar to observations at −15 °C for a melting ratio of 0.28. At $T_\infty = -15\ ^\circ\mathrm{C}$ and $m_r = 0.12$ only a thin rime type ice accretion layer occurs. After 120 s, no characteristic wedge has developed.

Fig. 39 shows comparisons between numerically and experimentally predicted accretion shapes for $m_r = 0.12$ after 120 s of icing. The conclusions are similar to those given for $m_r = 0.28$. The predicted ice shapes are globally overestimated compared to the experimental ones, but the model is able to predict the decrease of $\alpha_0$ for low melting ratios (from $m_r = 0.28$ to $m_r = 0.12$, see Fig. 29). As for $m_r = 0.28$ IGLOO2D strongly overestimates accretion growth at −15 °C because water freezing and particle sticking is not balanced properly. Fig. 40 gives an additional overview on the influence of melting ratio for $T_\infty = 0\ ^\circ\mathrm{C}$. Increasing $m_r$ from 0.12 to 0.28 yields a more voluminous ice accretion at a constant total water content of $12\ \mathrm{g/m^3}$. A further increase in melting ratio to $m_r = 0.5$ results in a decrease of ice accretion size. It has to be kept in mind that in case of $m_r = 0.5$ the TWC has been almost halved to $6.4\ \mathrm{g/m^3}$. According to Fig. 28(b) the accretion efficiency drops from 0.41 to 0.28 which is about 32% if one increases $m_r$ from 0.28 to 0.5 at $T_\infty = 0\ ^\circ\mathrm{C}$. The model is able to predict the decrease of $\alpha_0$ from $m_r = 0.28$ to $m_r = 0.5$ as well. Indeed, for high $m_r$, the wall liquid mass fraction $y_l$ increases, which enhances the erosion rate $\epsilon_{er}$ (Eq. (14)).

So far only accretion images of the NACA 0012 airfoil have been discussed. Fig. 41 shows ice accretions on the cylinder obtained at melting ratios of 0.12. The accretion shapes are very similar to the iced NACA 0012 airfoil in Fig. 38. Again, maximum icing severity is given at $T_\infty = 0\ ^\circ\mathrm{C}$ where no shedding occurs for $m_r = 0.12$. At −5 °C, the accretion develops very straight slopes of almost no curvature. Similar to the NACA 0012 airfoil only very little accretion can be observed for $T_\infty = -15\ ^\circ\mathrm{C}$. Comparisons between simulations and experiments are shown in Fig. 42. Conclusions are similar to those drawn for the NACA 0012 profile. For $T_\infty = 0\ ^\circ\mathrm{C}$ and $T_\infty = -5\ ^\circ\mathrm{C}$, the accuracy of $t_L$-computation is moderate

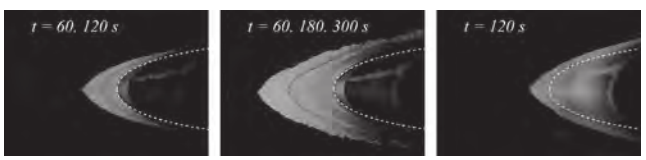


(a) $T_\infty = 0^\circ\ C$ (b) $T_\infty = -5^\circ\ C$ (c) $T_\infty = -15^\circ\ C$

**Fig. 36.** NACA 0012: Side view ice accretion shapes at $TWC = 12\ \mathrm{g/m^3}$ and $m_r = 0.28$, variation of temperature.

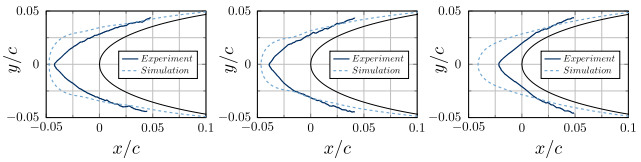


(a) $T_\infty = 0^\circ\ C$ (b) $T_\infty = -5^\circ\ C$ (c) $T_\infty = -15^\circ\ C$

**Fig. 37.** NACA 0012: Simulation versus experiment - side view ice accretion after 120 s at $TWC = 12\ \mathrm{g/m^3}$ and $m_r = 0.28$, variation of temperature.

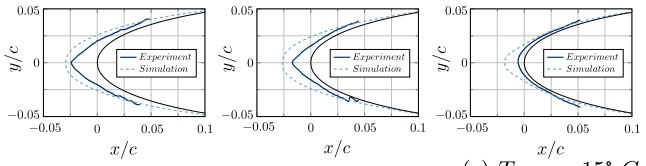


(a) $T_\infty = 0^\circ\ C$ (b) $T_\infty = -5^\circ\ C$ (c) $T_\infty = -15^\circ\ C$

**Fig. 39.** NACA 0012: Simulation versus experiment - side view ice accretion after 120 s of icing at $TWC = 12\ \mathrm{g/m^3}$ and $m_r = 0.12$.

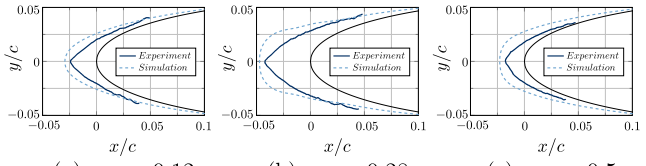


(a) $m_r = 0.12$ (b) $m_r = 0.28$ (c) $m_r = 0.5$

**Fig. 40.** NACA 0012: Simulation versus experiment-side view ice accretion after 120 s of icing at $T_\infty = 0\ ^\circ\mathrm{C}, TWC = 12\ \mathrm{g/m^3}$ for (a) and (b) and $TWC = 6.4\ \mathrm{g/m^3}$ for c).

(about 20 and 30% overestimation) but the accretion shape is not well matched. The upper and lower limits of the ice shapes are well predicted. The trend to overestimate the ice shape at the lower temperature $-15\ ^\circ\mathrm{C}$ is more pronounced for the cylinder profile. Once again, the sticking efficiency model (Eq. (8)) is not able to counterbalance the large freezing mass rate at low temperature. The diameter of the cylinder is 6 cm which is far smaller than the typical profiles from which the laws for the equivalent sand grain roughness used in the computation of the rough heat transfer coefficients $h_t$ have been derived (typical 1 m chord profiles). The model for the equivalent sand grain roughness is used out of the applicable ranges for the cylinder. Thus, a bad estimation of $h_t$ has a direct influence on $f_l$ via the Messinger energy balance and then on both the freezing mass rate and the sticking efficiency. This may explain the larger discrepancies between the numerical and the experimental ice shapes for the cylinder.

Additional images of mixed phase ice accretion of the NACA 0012 airfoil at $m_r = 0.12$ are shown in Fig. 43. No black aluminum tape is applied to the airfoil surface. At $T_\infty = 0\ ^\circ\mathrm{C}$ one can observe a wedge-shaped mixed phase ice accretion spanning among the total center body of the airfoil model. The stagnation line of the ice accretion features a clear and sharp edge. The accretion structure can be described as glassy and it is soaked with liquid water. The accretion composite is very cohesive, minor plastic deformation affected by the ambient airflow is plausible. The accretion ends with a zone of irregular structure. Single sheets of ice are dragged downstream by shear stresses of the airflow, according to observations in the topview image of Fig. 34 for $m_r = 0.28$. At $T_\infty = -5\ ^\circ\mathrm{C}$ the effective mixed phase ice accretion wedge looks rather similar to the accretion at $0\ ^\circ\mathrm{C}$. In the downstream region solid roughness elements can be observed as they appeared also for $m_r = 0.28$ in Fig. 35. At $-5\ ^\circ\mathrm{C}$ the ice accretion strongly adheres to the airfoil and is less deformable. Both accretion of Fig. 43 can be categorized as glaze ice accretions according to the classification of the COX experiments, cf. Fig. 5(a).

At $T_\infty = -15\ ^\circ\mathrm{C}$, the ice accretion can be considered as rime type ice according to COX classifications. Fig. 44 shows front side images of the cylinder model exposed to mixed phase clouds at $-15\ ^\circ\mathrm{C}$ with $m_r = 0.12$ and 0.28 respectively. The ice accretions are very dry and have a milky appearance indicating a high amount of incorporated air.

So far, ice accretion images have been presented for low and moderate melting ratios of 0.12 and 0.28 respectively. Fig. 45 shows side view images of cylinder ice accretions for a melting ratio of 0.5 at static temperatures of $0\ ^\circ\mathrm{C}$ and $-5\ ^\circ\mathrm{C}$. At $0\ ^\circ\mathrm{C}$ the accretion features a smooth surface of significant curvature which merges tangentially with the cylinder surface. After 180 s, the accretion tends to detach but does not shed. The reason is that a part of the accretion adheres strongly to the hemispherical tail end of the cylinder model. At $T_\infty = -5\ ^\circ\mathrm{C}$ the ice accretion shape is affected by liquid water freezing. The accretion features a higher volume compared to $T_\infty = 0\ ^\circ\mathrm{C}$ and does not merge smoothly with the cylinder surface. Liquid film freezing particularly occurs for circumferential angles in the range of 45° to 90°. The slopes of the ice accretion are rather straight lines. Anyway, the accretion tip is not very sharp as significant film freezing occurs downstream of the stagnation point.

Fig. 46 compares numerically and experimentally predicted ice accretions at melting ratios of 0.5. Figs. 27 and 28(a) show that $m_r = 0.5$ corresponds to the right part of the plateau effect where $\alpha_0$ decreases for high $m_r$. Fig. 29 shows that the tendency is similar for the IGLOO2D simulations at $m_r = 0.5$ except for the cylinder where the decrease of $\alpha_0$ for high $m_r$ has just begun at $m_r = 0.5$. This can explain why the predicted ice shapes are overestimated compared to the experimental ones for the cylinder.

All ice accretions on the NACA 0012 airfoil shown so far have been obtained at an angle of attack of 0°. Accretion tests have also been performed with the airfoil inclined at an angle of attack of −8°. Fig. 47 shows corresponding side view images for $m_r$ = 0.12 and 0.28 obtained at $T_\infty = -5\ ^\circ\mathrm{C}$. It has to be mentioned that the suction side corresponds to the lower side of the airfoil as the airfoil has been aligned with a negative angle of attack. Lasersheet visualisation indicates that liquid film flow and particle reimpact on the pressure side strongly affects accretion growth as illustrated

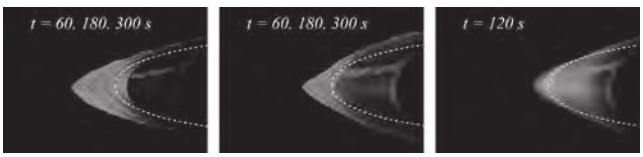


(a) $T_\infty = 0^\circ\ C$ (b) $T_\infty = -5^\circ\ C$ (c) $T_\infty = -15^\circ\ C$

**Fig. 38.** NACA 0012: Side view ice accretion shapes at $TWC = 12\ \mathrm{g/m^3}$ and $m_r = 0.12$, variation of temperature.

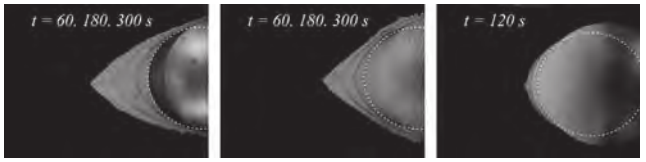


(a) $T_\infty = 0^\circ\ C$ (b) $T_\infty = -5^\circ\ C$ (c) $T_\infty = -15^\circ\ C$

**Fig. 41.** Cylinder: Side view ice accretion shapes at $TWC = 12\ \mathrm{g/m^3}$ and $m_r = 0.12$, variation of temperature.

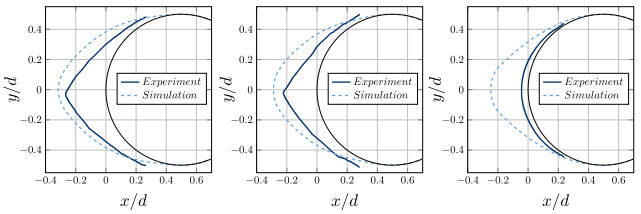


(a) $T_\infty = 0^\circ\ C$ (b) $T_\infty = -5^\circ\ C$ (c) $T_\infty = -15^\circ\ C$

**Fig. 42.** Cylinder: Simulation versus experiment - side view ice accretion after 120 s at $TWC = 12\ \mathrm{g/m^3}$ and $m_r = 0.12$, variation of temperature.

in Fig. 47. With the ice accretion propagating towards the airfoil tip, the stagnation point position also changes. A separation bubble develops on the suction side where liquid water accumulates. Ice particle sticking is benefited resulting in local ridges. These complicated growth mechanisms cannot be reproduced by IGLOO2D. Anyway, from a qualitative point of view the simulations correctly locate the ice accretions on the pressure side of the airfoil, see Fig. 48. For melting ratios higher than 0.28 only thin accretion layers develop which are dragged towards the suction side in the direction of airflow circulation.

### 4.4. Variation of total water content

In the previous test cases, the total water content has been kept constant at $TWC = 12\ \mathrm{g/m^3}$ except for $m_r = 0.5$. This section focuses on the influence of TWC variation on ice accretion growth at constant melting ratio. According to Fig. 8 the operational range of the IWT allows total water content variation from of 7.3 to 17 $\mathrm{g/m^3}$ at $m_r = 0.2$.

Fig. 49(a) shows plots of ice accretion thickness $t_L$ in the stagnation point obtained after 120 s of icing for both test articles at $T_\infty = 0\,^\circ\mathrm{C}$ and $T_\infty = -5\,^\circ\mathrm{C}$. Overall, the dependence between $t_L$ and TWC can be considered as rather linear. Except for the ice accretion on the cylinder at $T_\infty = -5\,^\circ\mathrm{C}$, a decent saturation effect can be observed, however. The plots have an inflexion point at $TWC = 12\ \mathrm{g/m^3}$ and show a decreasing gradient for higher total

(a) $T_\infty = 0^\circ\ C$

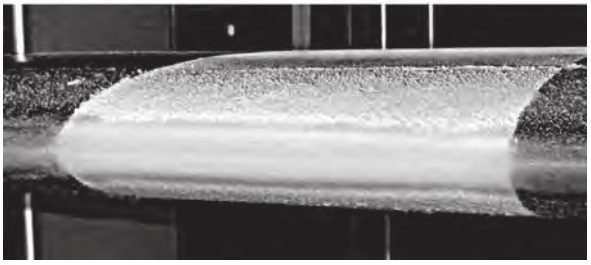

(b) $T_\infty = -5^\circ\ C$

**Fig. 43.** NACA 0012: Ice accretion surface structure at $m_r = 0.12, TWC = 12\ \mathrm{g/m^3}$ obtained after 120 s of icing.

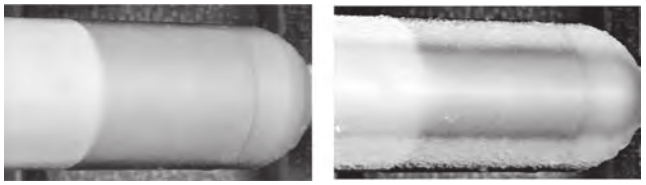

(a) $m_r = 0.12$ (b) $m_r = 0.28$

**Fig. 44.** Cylinder: Ice accretion surface structure at $T_\infty = -15^\circ C, TWC = 12\ \mathrm{g/m^3}$ obtained after 120 s of icing.

water contents. It can be concluded that $TWC = 12\ \mathrm{g/m^3}$ is a critical value where maximum sticking ability is given, at least for the first 120 s of ice accretion.

This conclusion is partly confirmed by Fig. 49(b) which shows the dependency of stagnation point accretion efficiency $\alpha_0$ on total water content. Only for the NACA 0012 at $-5\,^\circ\mathrm{C}$ and for the cylinder at $0\,^\circ\mathrm{C}$ the peak value appears at $TWC = 12\ \mathrm{g/m^3}$. In this context it has to be mentioned that the determination of accretion efficiency is somewhat sensitive to angle determination and collection efficiency calculation. Overall, the accretion efficiency can be considered as rather constant for each condition of TWC variation.

Side view images of ice accretion on the NACA 0012 airfoil are shown in Fig. 50 for total water contents of 7.3, 12 and 17 $\mathrm{g/m^3}$ at $T_\infty = 0\,^\circ\mathrm{C}$. The images (a) and (b) show super-imposed ice accretion shapes obtained after 60 and 120 s of icing. In both images ice accretions for TWC = 7.3, 12 and 17 $\mathrm{g/m^3}$ are included. The images give the impressions of accretion growth at constant TWC for various time steps, thus indicating a correlation between accretion time and TWC. In Fig. 50(c) accretion shapes are superimposed for adapted times of ice accretion growth. The time has been adapted in a way that for three TWC conditions the total mass of ice and water which has impinged on the airfoil is the same. In other words: Ice accretion shapes are compared for different combinations of $TWC \cdot time = constant$. The edges of all three ice accretions are almost congruent.

Finally, a comparison between the numerical and experimental results regarding TWC variation is given by Fig. 51. Ice accretion shapes resulting from mixed phase icing of the NACA 0012 airfoil at $T_\infty = 0\,^\circ\mathrm{C}$ are plotted. A very good agreement between the experimentally and numerically predicted accretion shapes can be observed, indicating that TWC dependence of ice accretion growth is captured very well by IGLOO2D. Also in NRC studies [18], the accretion efficiency near the stagnation point turned out to be independent of *TWC*. It follows that the accretion growth rate $\dot{t}_l$ linearly depends on *TWC* which is respected in IGLOO2D (Eq. (20)).

The present studies have shown a rather linear dependence of accretion growth rate on total water content. Again, it has to be stressed that TWC has only been varied at a constant melting ratio

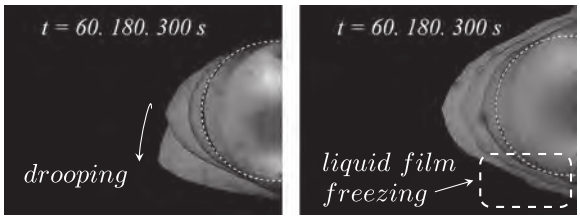


(a) $T_\infty = 0^\circ\ C$ (b) $T_\infty = -5^\circ\ C$

**Fig. 45.** Cylinder: Ice accretion shape depending on temperature, $TWC = 6.8\ \mathrm{g/m^3}$ and $m_r = 0.5$.

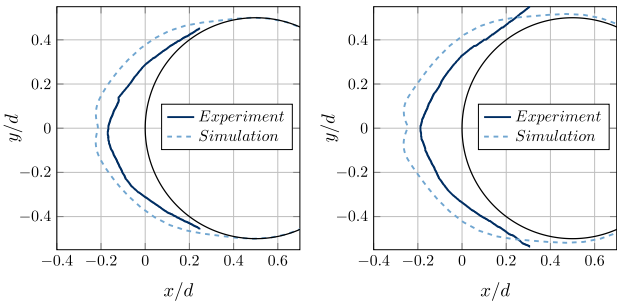


**Fig. 46.** Cylinder: Simulation versus experiment - side view ice accretion after 120 s at $TWC = 6.8$ g/m$^3$ and $m_r = 0.5$, variation of temperature.

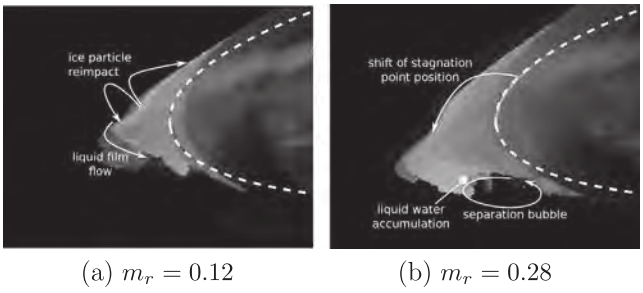


**Fig. 47.** NACA 0012: Inclined airfoil, $\alpha = -8°, T_\infty = -5$ °C, variation of melting ratio $m_r$.

of 0.2 for a single particle size distribution. Even if a similar dependency is expected for higher melting ratios it cannot be generalized based on the available data. In contrast to NRC observations, no cessation of ice accretion growth (steady state shape) has been observed at low total water contents of about 7 g/m$^3$, also for higher melting ratios up to 0.6.

### *4.5. Correlation of particle sticking and accretion shape*

The photographic side view images presented in Sections 4.1–4.4 offer good impressions of ice accretion growth as they include accretion shapes for different points in time. A detailed look on accretion growth characteristics shall be given in this section. Special focus will be set on the accretion growth rate depending on the ice accretion geometry.

Fig. 52 includes time histories of accretion thickness $t_L$ for the cylinder model. Results are shown for temperatures of 0 °C and −5 °C as well as for melting ratios of 0.12, 0.28 and 0.5. While the TWC has been kept constant at 12 g/m$^3$ for $m_r = 0.12$ and $m_r = 0.28$, it has been decreased to TWC = 6.8 g/m$^3$ at $m_r = 0.5$

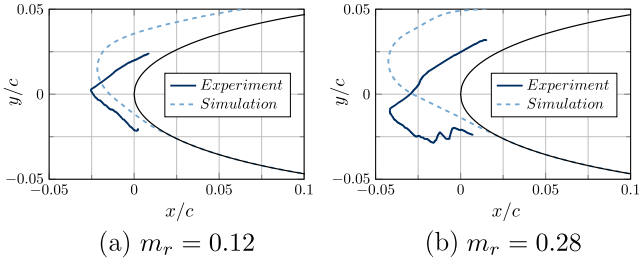


**Fig. 48.** NACA 0012, simulation vs. experiment: Side view ice accretion after 120 s, inclined airfoil, $\alpha = -8°$, $T_\infty = -5$ °C, variation of melting ratio $m_r$.

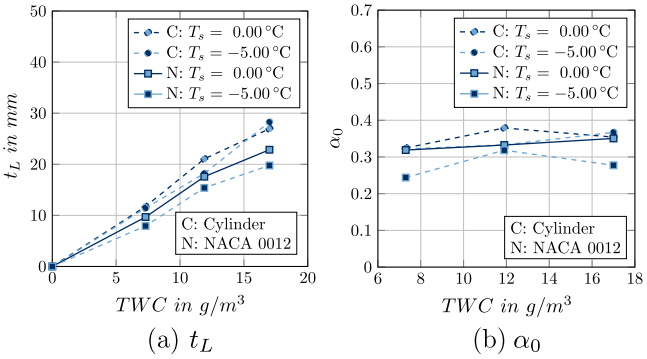


**Fig. 49.** Ice particle sticking depending on total water content, $t_L$ and $\alpha_0$ obtained for 120 s of icing at $m_r = 0.2$.

as explained in Section 2.2. The accretion growth rate $\dot{t}_L$ corresponds to the time-derivative of the accretion thickness $t_L$, see Fig. 22. For all cases it can be observed that the accretion growth rate tends towards steady state conditions. Steady state growth rates are highlighted by dashed linear slopes. Highest growth rates can be observed at $m_r = 0.28$ for both temperatures which agrees with the maximum sticking efficiencies in Fig. 27 for this melting ratio. At $T_\infty = 0$ °C accretion shedding can be observed for $m_r = 0.28$. It is worth mentioning that the accretion thickness almost reaches the same size for both shedding events detected. Also at $m_r = 0.5$ the ice accretion tends to detach from the cylinder surface but does not totally shed, see Fig. 45. At $T_\infty = -5$ °C very similar growth rates can be observed for $m_r = 0.12$ and 0.5. In case of $m_r = 0.12$, accretion growth is restricted by limited particle sticking. For $m_r = 0.5$ rather high accretion efficiencies of about 0.4 have been observed but the growth rate is limited by the low TWC of 6.8 g/m$^3$.

The plots in Fig. 52 show that the accretion growth rate $\dot{t}_L$ decreases with time until a steady state value is reached. This time dependence must be correlated to the accretion efficiency which decreases as the ice accretion shape changes in time.

A characteristic geometric attribute is the accretion tip angle $\varphi_0$, see Fig. 14. Fig. 53 shows the deviation of $\varphi_0$ in time, the test conditions correspond to the plots of $t_L$ in Fig. 52. The solid lines are exponential fits of scattered data based on Eq. (21). Due to the accretion curvature, no angles are detected in the range of $160° < \varphi_0 < 180°$. Detailed information on the accretion detection code and the method of accretion angle determination can be found in the work of Traub [49].

$$\varphi_0(t) = a \cdot e^{(b \cdot t + c)} + d \tag{21}$$

In Fig. 53 it can be observed that the accretion angle decreases for all melting ratios, the strongest gradient appears for $m_r = 0.12$. The accretion angles in Fig. 53 converge towards steady state values (coefficient *'d'* in Eq. (21)) as indicated by dashed lines in the graph. In this context, a correlation between the accretion growth rate $\dot{t}_L$ and the accretion angle $\varphi_0$ can be found. As the accretion angle decreases towards a constant value, the growth rate does as well.

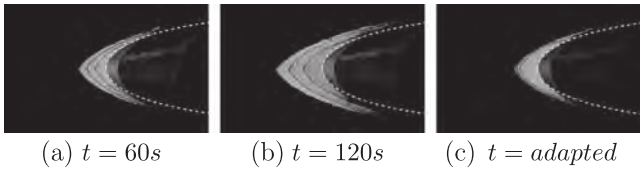


**Fig. 50.** NACA 0012: Side view ice accretion, TWC dependency, $T_\infty = 0$ °C, $m_r = 0.2$.

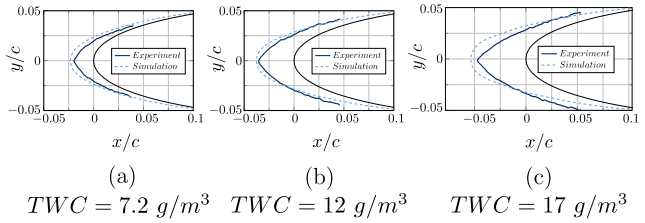


**Fig. 51.** NACA 0012: Simulation vs. experiment - Side view ice accretion after 120 s, $T_\infty = 0\,^\circ$C, $m_r = 0.2$, variation of total water content.

The reduction of accretion growth rate can be addressed to two factors of influence.

First, the stagnation point collection efficiency $\beta_0$ decreases for sharper accretion angles as the increment impact area *ds* increases, see Fig. 22. Second, the ability of particle sticking is limited by its impact angle. In case of a flat-angle impact, the particle rebounds due to its high momentum tangential to the accretion surface. On the contrary, a rather vertical impact implies a high normal component of impact velocity benefiting particle fragmentation and sticking. The impact angle is taken into account in the erosion model (Eq. (14)) as it explicitly depends on the mean tangential velocity of the impinging ice crystals $V^t_{imp,c}$. On the other hand, the model for the sticking efficiency $\epsilon_s$ (Eq. (8)) does not depend on the impact angle as it does not take into consideration the local normal vector to the wall. An analogy with the impingement of Supercooled Large Droplets (SLD) may be used to derive such correlations for the ice crystals. Dedicated academic databases are not available yet to tackle this open key point. Steady state tip angles of growing ice accretions have also been observed in NRC studies and the aspect of angular dependency on accretion efficiency is discussed by Currie [17,18]. He points out that $\varphi_0$ stops changing when local material losses due to accretion erosion and particle rebound reach a maximum and so the accretion efficiency $\alpha_0$ reaches a minimum [17]. A minimum is possible for $0^\circ \leqslant \alpha_0 \leqslant 90^\circ$ when erosion is assumed to be a function of the normal velocity component (as appropriate for a brittle material) as well as the tangential, in contrast to the current erosion model in ACCRET2D which uses only the latter [17].

Fig. 53 indicates differences of steady state accretion angle depending on melting ratio in the present study. In case of $T_\infty = -5\,^\circ$C the lowest steady state angle appears to be about 80° for $m_r = 0.12$, indicated by the dashed line asymptote. In contrast, a rather obtuse angle of 130° appears for $m_r = 0.5$. As discussed by Currie, the steady state angles result from a balance of local mass fluxes. Based on accurate observations of side view video sequences it is supposed that in the current study the accretion surface is deformed by the ambient flow field. Shear stresses seem to homogenise the accretion surface by dragging an ice/water mixture in downstream direction. This kind of surface flow seems to be most dominant at high melting ratios, when significant liquid is available on the accretion surface. Thus, it is hypothesized that the obtuse angle of 130° at $m_r = 0.5$ is significantly affected by a shear stress-driven transport of ice-water mixture towards the base of the accretion wedge. Such transport avoids the formation of a sharp accretion angle and reduces the accretion efficiency by conveying lose ice particles in downstream direction. This aspect is not respected in the current version of IGLOO2D. At rather dry conditions of $T_\infty = -5\,^\circ$C and $m_r = 0.12$, shear stress-driven transport is less severe and a sharp accretion angle develops, mostly affected by particle sticking limitations. This aspect, ice particle sticking limitation depending on impact angle is restated later in the text.

Further time histories of accretion thickness $t_L$ and tip angle $\varphi_0$ are shown in Fig. 54. The plots represent icing of the NACA 0012 airfoil at $m_r = 0.2$ and $T_\infty = 0\,^\circ$C. Total water content has been varied between 7.3 and 17 g/m$^3$ according to Section 4.4. One can clearly observe an increase in growth rate for higher TWCs. Steady state growth conditions have been established after about 120 s for all test runs. It is interesting to observe, that the steady state accretion angle decreases for higher TWC. Based on comparisons to other test runs this observation cannot be generalized.

The time histories of $t_L$ and $\varphi_0$ presented in Sections 4.3 and 4.4 indicate a strong connection between accretion growth rate $\dot{t}_L$ and accretion angle $\varphi_0$. Moreover, a strong dependence of $\dot{t}_L$ and $\varphi_0$ on temperature has been observed.

To further emphasize the correlation between particle sticking and impact angle, plots of accretion efficiency $\alpha_0$ against accretion angle $\varphi_0$ are shown in Figs. 55 and 56. Based on the assumption that erosion has no first order effect, it is supposed that the correlation of accretion efficiency and accretion angle can be transferred to the ice particle sticking ability depending on impact angle. Fig. 55 represents cylinder icing at 0 °C and −5 °C with TWC variation in the range of 7.3–17 g/m$^3$ according to Section 4.4. For $T_\infty = 0\,^\circ$C, all plots of $\alpha_0$ against $\varphi_0$ run rather congruent to each other. For $T_\infty = -5\,^\circ$C, the plots converge towards a common slope for accretion angles below 120°. It can be concluded that for $T_\infty = 0\,^\circ$C particle sticking is rather independent of total water content on the cylinder. For a given impact angle, the accretion efficiency $\alpha_0$ is almost equal for all three plots of Fig. 55(a). At $T_\infty = -5\,^\circ$C however, better sticking is given for increased TWCs at impact angles higher than 60° ($\varphi_0 > 120^\circ$).

Fig. 56 shows further plots of $\alpha_0$ against $\varphi_0$ but with focus on melting ratio variation. Again, results are shown for mixed phase icing of the cylinder at $T_\infty = 0\,^\circ$C and $T_\infty = -5\,^\circ$C. Similar to

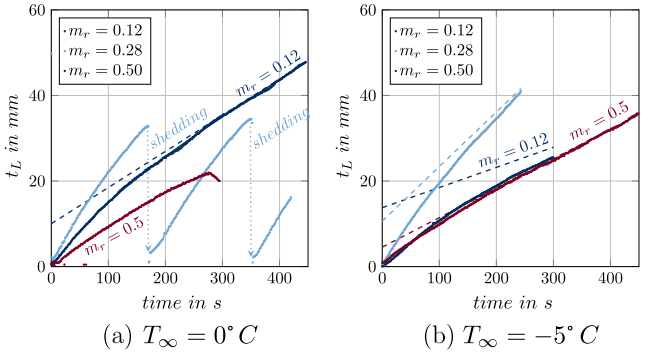


**Fig. 52.** Cylinder: Time history of leading edge accretion thickness $t_L$, variation of melting ratio $m_r$.

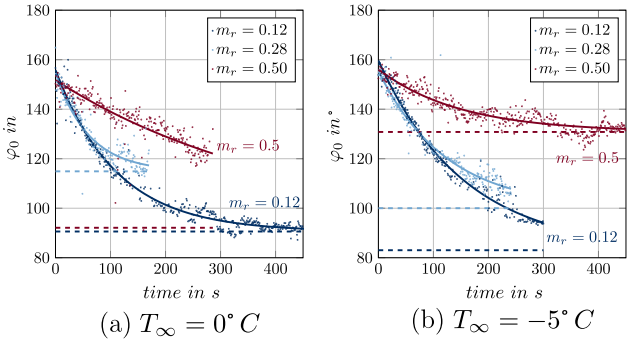


**Fig. 53.** Cylinder: Time history of leading edge accretion angle $\varphi_0$, variation of melting ratio $m_r$.

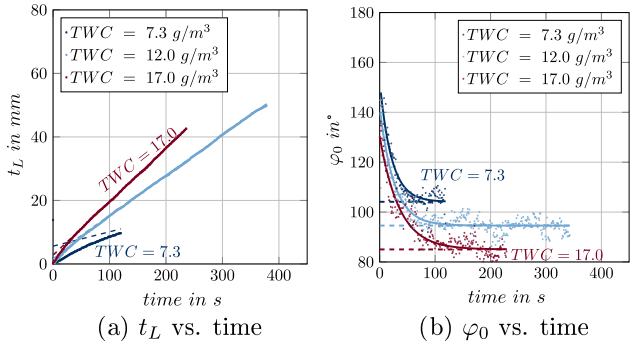


**Fig. 54.** NACA 0012: Time history of leading edge accretion thickness $t_L$ and accretion angle $\varphi_0$, $T_\infty = 0\,°C$ variation of total water content *TWC*.

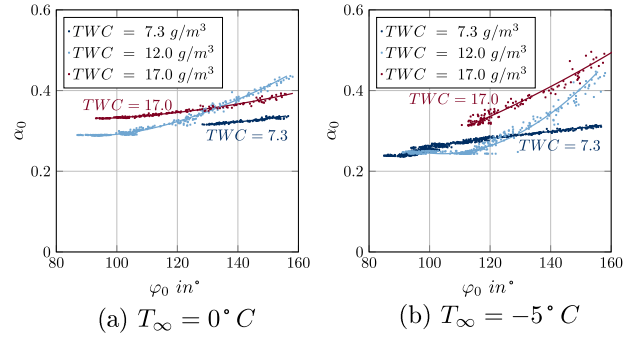


**Fig. 55.** Cylinder: Accretion efficiency $\alpha_0$ depending on accretion angle $\varphi_0$, variation of total water content *TWC*.

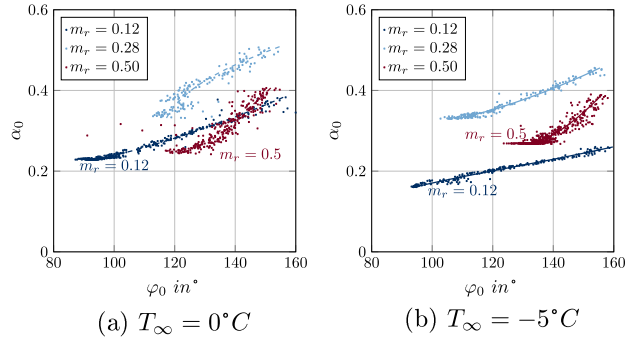


**Fig. 56.** Cylinder: Accretion efficiency $\alpha_0$ depending on accretion angle $\varphi_0$, variation of melting ratio $m_r$.

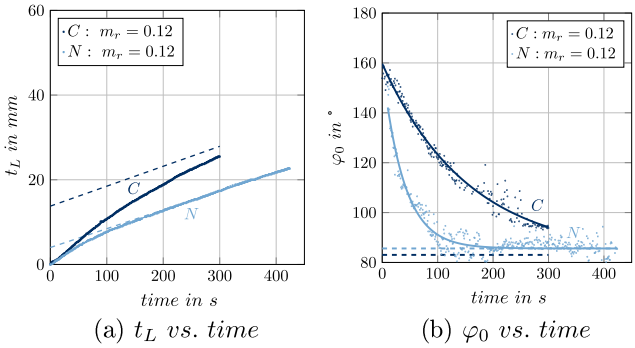


**Fig. 57.** Cylinder and NACA 0012: Time history of leading edge accretion thickness $t_L$ and accretion angle $\varphi_0$, $T_\infty = -5\,°C$.

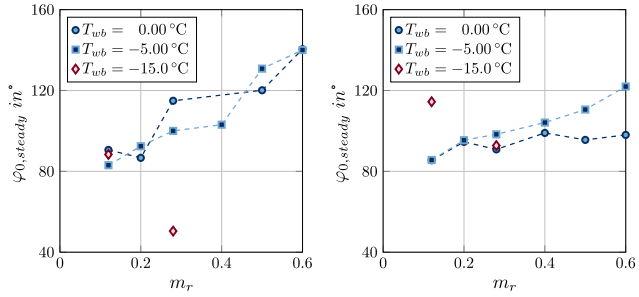


**Fig. 58.** Steady state accretion angle $\varphi_{0,steady}$ depending on melt ration $m_r$.

Fig. 55, accretion efficiency decreases for lower accretion angles. The more particle impingement deviates from a normal impact, the less is its tendency to stick to the accretion surface. For 0 °C and −5 °C highest sticking ability is given for a melting ratio of 0.28. At 0 °C the corresponding plot of $m_r = 0.28$ features a concave curvature towards a steady state angle of about 120°. It has to be pointed out that shedding occurred after 160 s and that an accretion angle even lower than 120° might develop if the accretion would continue growing. Regarding the plot of $m_r$=0.5 at $T_\infty = 0\,°C$ in Fig. 56(a) it has to be kept in mind that the accretion droops after 180 s, see Fig. 45, thus making the detection of accretion angle inaccurate. For $m_r = 0.12$ significantly lower sticking ability is given for $T_\infty = -5\,°C$ compared to $T_\infty = 0\,°C$. This observation is in agreement with the side view images of Fig. 41 which show the largest ice accretions at $T_\infty = 0\,°C$. Again it shall be stressed that the steady state angles identified in Figs. 53 and 54 do not represent critical angles for particle sticking. Otherwise accretion tip growth would stop and steady state wedges of constant angle would develop as discussed in more detail by Baumert [44]. Steady state growth conditions are characterized by a balance of local mass fluxes and it is supposed that in the present study a surface flow of lose ice/water mixture significantly contributes to this balance, especially for high melting ratios.

Finally, a comparison between mixed phase icing of the cylinder model and the NACA 0012 airfoil shall be drawn. Fig. 57 shows time histories of $t_L$ and $\varphi_0$ of the cylinder and the NACA 0012 model at $m_r$=0.12. It turns out that the accretion growth rate and angle converge towards the same values for both models. However, steady state conditions are reached first for the NACA 0012 airfoil. The airfoil has a smaller leading edge diameter of 15.8 mm compared to the cylinder diameter of 60 mm. Consequently, the accretion reaches its steady state angle at a lower accretion thickness $t_L$ and thus earlier in time. On the contrary, this means that the accretion angle of the cylinder takes longer to reach steady state conditions so that the accretion tip grows at a higher rate for a long period of time. This explains why higher accretion efficiencies have been obtained for the cylinder model compared to the NACA 0012 airfoil in Figs. 27 and 28 at low and moderate melting ratios. The accretion efficiencies have been averaged over 120 s of icing. In this period of time $\dot{t}_L$ is constantly higher for the cylinder model than for the NACA 0012 airfoil resulting in higher accretion efficiencies of the cylinder.

Fig. 57 has shown good agreement between the steady state accretion angles of the cylinder model and the NACA 0012 airfoil for $m_r = 0.12$. Fig. 58 gives an overview of steady state accretion angles over the whole range of melting ratios investigated. For a static air temperature of −5 °C one can observe a continuous increase of steady state angle with melting ratio. There is rather good agreement between the cylinder and NACA 0012 model except for melting ratios of 0.5 and 0.6 where higher values of $\varphi_0$ have been determined for the cylinder. For $T_\infty = 0\,°C$ the

informative value of Fig. 58 is limited as ice accretion drooping and shedding occurs for melting ratios higher than 0.2. The accretion angle can consequently not properly be detected, especially for the cylinder, see Fig. 45(a). At $T_\infty = -15\,^\circ\mathrm{C}$ and $m_r = 0.28$ the decrease of $\varphi_0$ is rather constant in time during the 120 s of the test run. In consequence, the evaluation software predicts a very low steady state angle of about 50° for the cylinder model.

## 5. Conclusions

Based on the results discussed in Section 4 it can be summarized that mixed phase ice accretion growth strongly depends on temperature, melting ratio and TWC. NRC studies have also emphasized a strong influence of Mach number and particle size as explained in chapter 1. Moreover, a time dependency of accretion growth rate $\dot{t}_L$ could be observed.

This dependency can be addressed to the change of accretion shape in time. Mixed phase ice accretions typically develop a wedge shape because the local particle collection- and accretion efficiency depends on the impact angle. Initially, maximum growth rates occur in the stagnation point region where higher impingement angles and collection efficiencies occur compared to the outer region of the ice accretion. Consequently, best local growing conditions are given at the tip of the ice accretion. A sharp wedge develops and the impact conditions in the stagnation point region change. The collection efficiency $\beta_0$ decreases because the accretion slopes decline and the particles impinge on a broader effective area. Also the particle sticking ability decreases, as the tangential component of impact velocity rises. Possibly erosion increases, which is not indicated by IGLOO2D for the low Mach number conditions of the present study, however. Finally, steady state growth conditions are reached by a balance of local mass fluxes, characterized by a steady state accretion tip angle $\varphi_0$ and growth rate $\dot{t}_L$.

It is assumed that erosion effects become more significant at enhanced Mach numbers. This assumption is indicated by the discrepancies of the numerically predicted ice shapes compared to the experiments as discussed in Section 4. While the accretion growth rate $\dot{t}_L$ is matched pretty well in the simulations for $T_\infty = 0\,^\circ\mathrm{C}$ and $T_\infty = -5\,^\circ\mathrm{C}$, the wedge-shaped accretion geometry is not exactly reproduced. IGLOO2D is calibrated based on NRC experiments performed at higher Mach numbers of 0.25 and 0.4 with smaller particles. Assuming the calibration is valid for the different conditions in this research, the discrepancy of accretion shape in this study indicates that erosion effects play no significant role at rather low Mach numbers of 0.12.

In consequence, the discrepancy of numerically and experimentally predicted ice shapes emphasizes a correlation between particle sticking and impact angle for low Mach number conditions. It is hypothesized that in the present study also restructuring of the accretion surface, induced by shear stresses of the ambient flow field, affects the accretion shape, at least at high $m_r$. Both aspects are not respected in the current version of IGLOO2D. At the accretion tip a balance of mass flows resulting from erosion, surface flow and particle sticking is supposed to cause a constant tip angle. The accretion keeps growing however, because the tip angle never reaches a critical value for particle sticking. In this context, it has to be stressed that it is difficult to differentiate between sticking and erosion effects regarding the shaping of mixed phase ice accretions.

A next step towards mixed phase ice accretion modelling would be to connect real ice particle impact behaviour to sticking ability and erosion effects in the accretion model. Also dragging of the ice water/mixture along the accretion surface by ambient air should be respected. At current state, experimental data on this topic is limited. Especially, ice particle impact on real mixed phase ice accretion surfaces at various cloud conditions has not been studied systematically yet. Complementary high speed investigations to this study have been conducted, in which ice particle impact during mixed phase ice accretion growth has been recorded [44]. The tests have been performed in rather short term and data is limited. Anyway, the impact sequences indicate that particle sticking is strongly dependent on surface roughness for low Mach number conditions.

One of the main outcomes of the present study is a strong temperature influence on the ice accretion process. The accretion efficiency $\alpha_0$ decreases for lower temperatures. The reason can primary be found in the reduction of available liquid due to freezing and thus losses in sticking ability. It has to be pointed out that the temperature effect is not in agreement with NRC studies where partly higher accretion efficiencies have been determined at temperatures significantly below the freezing point than for $T_{wb} > 0\,^\circ\mathrm{C}$ [17,18]. This discrepancy can possibly be explained by a freezing fraction of the injected droplets close to unity in case of the NRC studies which is much higher than in the present study.

In agreement with NRC studies, enhanced icing severity has been observed for increased total water contents in the present study. More ice accretes to the test model because effectively more particles impinge on the surface. The accretion efficiency keeps rather constant for a variation of TWC. In contrast to NRC studies lowering of TWC has not caused a stop of accretion growth, meaning the formation of steady state accretion geometries.

All accretion geometries obtained in the present study can be described as wedge-shaped except for $T_\infty = -15\,^\circ\mathrm{C}$ and $m_r = 0.12$ where only a thin ice layer accreted. At $T_\infty = 0\,^\circ\mathrm{C}$ the accretion merges tangentially with the test article surface. In case of $T_\infty = -5\,^\circ\mathrm{C}$ an enhanced ice thickness occurs in the downstream region of the accretion because of liquid film freezing. Thus, an analogy to the mushroom accretion shapes yielded in NRC studies can be drawn even if the geometry is less pronounced in the current study. Roughness elements have been observed for $T_\infty = -5\,^\circ\mathrm{C}$ on the NACA 0012 airfoil surface induced by rivulet freezing. At $T_\infty = -15\,^\circ\mathrm{C}$ and $m_r = 0.28$ a solid wedge of straight slopes has been observed. Downstream of the wedge, large roughness elements can be found where liquid droplet freezing appears to be dominant.

A commonly discussed aspect of mixed phase ice accretion is the possibility of wedge shaping affected by the ambient flow field. Based on the results of the present study it can be claimed that a runback flow of ice/water-mixture is reasonable. However, total accretion deformation is rather implausible for mixed phase ice accretions at temperatures far below the freezing point. The accretion composite is very solid and not deformable, especially in case of the 'rime type' ice accretion at $-15\,^\circ\mathrm{C}$. For wet bulb temperatures above the freezing point slushy ice accretions occur and deformation might be more relevant. Thus, it would be interesting to determine material properties of ice accretions depending on the amount of incorporated water to assess the aspect of deformation. A measurement technique to determine the composition of ice accretions would have to be developed to perform such studies systematically. It has to be mentioned that tests of Currie et al. at $M = 0.65$ and $T_{wb} > 0\,^\circ\mathrm{C}$ have yielded accretion shapes with characteristic zones of constant accretion angle which are not consistent with appreciable material flow due to creep or viscoplasticity [17]. It is thus unlikely that significant deformation occurs for flow conditions of lower Mach number and dynamic pressure.

Ongoing works on IGLOO2D are now focusing on the improvement of the global accretion model proposed in this paper. Concerning the sticking efficiency model $\epsilon_s$, additional inputs with dimensionless numbers comparing the magnitude of the impinging kinetic energy to the magnitude of the energy required for

the ice crystals to be shattered during the impact should be taken into account. The models would be closely derived from those dedicated to the splashing phenomenon for Supercooled Large Droplets (SLD). To do this, dedicated academic experimental databases are required. Another difficulty is the quantitative influence of the wall liquid film on the ice crystal sticking efficiency $\epsilon_s$. The qualitative tendency is taken into account with the wall total liquid fraction $f_l$ as an input in the model for $\epsilon_s$, but once again, dedicated academic databases are necessary for a more quantitative understanding. Another significant way of improving the accretion model should focus on the runback model (Eq. (18)). More precisely, the computation of the part of the liquid water which has not frozen or evaporated and which actually runs back downstream or remains trapped inside the accreted ice is difficult. From our knowledge, there is no database dedicated to the study of this phenomenon. Ongoing works at ONERA are devoted to the computation of heat conduction inside both the test article and the ice layer resulting in melted zones from which ice shedding may be initiated.

## Conflict of interests

There are no conflict of interests existing.

## Acknowledgments

This project has received funding from the European Union's Seventh Framework Programm in research, technological development and demonstration under grant agreement n°ACP2-GA-2012-314314.

Many thanks go to Tom Currie from the National Research Council of Canada and to Kamel Al-Khalil from Cox & Company, Inc. for sharing experimental results presented in this paper. Special thanks belong to Hendrik Traub from TU Braunschweig for supporting the experimental studies of this paper with great efforts in the course of his student research project.

## References

[1] AGARD, Agard advisory report 334 - ice accretion simulation, Tech. rep., Advisory Group for Aerospace Research & Development, 1997.
[2] Aircraft Icing Handbook, Civial Aviation Authority of New Zealand, 2000.
[3] J. Mason, J. Strapp, P. Chow, The ice particle threat to engines in flight, in: 44th AIAA Aerospace Sciences Meeting and Exhibit, AIAA-2006-206, 2006.
[4] M. Grzych, J. Mason, Weather conditions associated with jet engine power-loss and damage due to ingestion of ice particles: what we've learned through 2009, in: 14th Conference of Aviation, Range and Aerospace Meteorology, 2010.
[5] A. Flegel, M. Oliver, Preliminary results from a heavily instrument engine ice crystal icing test in a ground based altitude test facility, in: 8th AIAA Atmospheric and Space Environmehts Conference, AIAA 2016-3894, 2016.
[6] M. Oliver, Validation ice crystal icing engine test in the propulsion system laboratory at NASA Glenn Research Center, in: 6th AIAA Atmospheric and Space Environments Conference, AIAA-2014-2898, 2014.
[7] D. Leroy, E. Fontaine, A. Schwarzenboeck, J. Strapp, L. Lilie, J. Delanoe, A. Protat, F. Dezitter, A. Grandin, HAIC/HIWC field campaign – specific findings on PSD microphysics in high IWC regions from in situ measurements: Median mass diameters, particle size distribution characteristics and ice crystal shapes, SAE technical paper 2015-01-2087, in: SAE 2015 International Conference on Icing of Aircraft, Engines and Structures, 2015.
[8] D. Leroy, E. Fontaine, A. Schwarzenboeck, J. Strapp, A. Korolev, G. McFarquhar, R. Dupuy, C. Gourbeyre, L. Lilie, A. Protat, J. Delanoe, F. Dezitter, A. Grandin, Ice crystal sizes in high ice water content clouds. part ii: Statistics of mass diameter percentiles in tropical convection observed during the HAIC/HIWC project, J. Atmos. Oceanic Technol. 34 (2017) 117–136.
[9] S. Bansmer, A. Baumert, S. Sattler, I. Knop, D. Leroy, A. Schwarzenboeck, T. Jurkat, C. Voigt, H. Pervier, B. Espositio, Design, construction and commissioning of the Braunschweig icing wind tunnel, Atmospheric Measurement Techniques, 2017 (under review).
[10] M. Feulner, S. Liao, B. Rose, X. Liu, Ice crystal ingestion in a turbofan engine, in: SAE 2015 International Conference on Icing of Aircraft, Engines and Structures, 2015.
[11] J. MacLeod, Development of ice crystal facilities for engine testing, in: SAE Aircraft & Engine Icing International Conference, 2007-01-3290, 2007.
[12] T. Currie, D. Fuleki, D. Knezevici, J. MacLeod, Altitude scaling of ice crystal accretion, in: 5th AIAA Atmospheric and Space Environments Conference, AIAA-2013-2677, 2013.
[13] P. Struk, T. Bartkus, J.-C. Tsao, T. Currie, D. Fuleki, Ice accretion measurements on an airfoil and wedge in mixed-phase conditions, in: SAE 2015 International Conference on Icing of Aircraft, Engines and Structures, 2015-01-2116, 2015.
[14] P. Struk, A. Broeren, J.-C. Tsao, M. Vargas, B. William, T. Currie, D. Knezevici, D. Fuleki, Fundamental ice crystal accretion physics studies, in: SAE 2011 Interlational Conference on Aircraft and Engine and Ground Deicing, SAE-2011-38-0018, 2011.
[15] P. Struk, T. Bencic, J.-C. Tsao, D. Fuleki, D. KKnezevici, Preparation for scaling studies of ice-crystal icing at the NRC research altitude test facility, in: 5th AIAA Atmospheric and Space Environments Conference, AIAA-2013-2675, 2013.
[16] T. Currie, P. Struk, D. Tsao, J-C. Fuleki, D. Knezevici, Fundamental study of mixed-phase icing with application to ice crystal accretion in aircraft jet engines, in: 4th AIAA Atmoshperic and Space Environments Conference, AIAA-2012-3035, 2012.
[17] T. Currie, D. Fuleki, Experimental results for ice crystal icing on hemispherical and double wedge geometries at varying mach numbers and wet bulb temperatures, 8th AIAA Atmospheric and Space Environmehts Conference, AIAA 2016-3740, 2016.
[18] T. Currie, D. Fuleki, A. Mahallati, Experimental studies of mixed-phase sticking efficiency for ice crystal accretion in jet engines, in: 6th AIAA Atmospheric and Space Environments Conference, AIAA-2014-3049, 2014.
[19] T. Currie, D. Fuleki, Development and application of an impedance-based instrument for measuring the liquid fraction and thickness of ice crystal accretions, in: SAE 2015 International Conference on Icing of Aircraft, Engines and Structures, 2015-01-2134, 2015.
[20] J. Mason, P. Chow, D. Fuleki, Understanding ice crystal accretion and shedding phenomenon in jet engines using a rig test, J. Eng. Gas Turbines Power 133 (2011), 041201–1 – 8.
[21] D. Kintea, Hydrodynamics and thermodanymics of ice particle accretion (Ph.D. thesis), TU Darmstadt, 2016.
[22] K. Al-Khalil, E. Irani, D. Miller, Mixed phase icing simulation and testing at the cox icing wind tunnel, in: 41st Aerospace Sciences Meeting and Exhibit, AIAA-2003-09-03, 2003.
[23] D. Miller, T. Bond, D. Sheldon, W. Wright, T. Langhals, K. Al-Khalil, H. Broughton, Validation of NASA thermal ice protection computer codes: Part 1-program overview, in: 35th Aerospace Sciences Meeting & Exhibit, AIAA-97-0049, 1997.
[24] T. Hauk, E. Bonaccurso, I. Roisman, C. Tropea, Ice crystal impact onto a dry solid wall. Particle fragmentation, Proc. R. Soc. A 471 (2015) 20150399.
[25] T. Hauk, Investigation of the impact and melting process of ice particles (Ph.D. thesis), Technische Universität Darmstadt, 2015.
[26] I. Roisman, C. Tropea, Impact of a crushing ice particle onto a dry solid wall, Proc. R. Soc. A 471 (2015) 20150525.
[27] R. Goodwin, D. Dischinger, Turbofan ice crystal rollback investigation and preparations leading to inaugural ice crystal engine test at NASA PSL-3 test facility, in: 6th AIAA Atmospheric and Space Environments Conference, AIAA-2014-2895, 2014.
[28] A. Griffin, D. Dicki, P. Lizanich, PSL icing facility upgrade overview, in: 6th AIAA Atmospheric and Space Environments Conference, AIAA-2014-2896, 2014.
[29] J. Veres, S. Jones, P. Jorgenson, Performance modeling of honeywell turbofan engine tested with ice crystal ingestion in the NASA propulsion system laboratory, In: SAE 2015 International Conference on Icing of Aircraft, Engines and Structures, 2015-01-2133, 2015.
[30] B. Messinger, Equilibrium temperature of an unheated icing surface as a function of air speed, J. Aerospace Sci. 20 (1953) 29.
[31] W. Wright, P. Jorgenson, J. Veres, Mixed phase modeling in glennice with application to engine icing, in: AIAA Atmospheric and Space Environments Conference, AIAA-2010-7674, 2010.
[32] W. Habashi, S. Nilamdeen, Multiphase approach toward simulating ice crystal ingestion in jet engines, J. Propul. Power 27 (5) (2011) 959–969.
[33] M. Rios Pabon, Ice crystal ingestion by turbofans (Ph.D. thesis), Drexel University, 2012.
[34] M. Oliver, Validation ice crystal icing engine test in the propulsion systems laboratory at NASA Glenn Research Center, in: 6th AIAA Atmospheric and Space Environments Conference, AIAA-2014-2898, 2014.
[35] P. Villedieu, P. Trontin, R. Chauvin, Glaciated and mixed phase ice accretion modeling using ONERA 2D icing suite, in: 6th AIAA Atmospheric and Space Environments Conference, AIAA-2014-2199, Atlanta, USA, 2014.
[36] P. Trontin, G. Blanchard, P. Villedieu, A comprehensive numerical model for mixed-phase and glaciated icing conditions, in: 8th AIAA Atmospheric and Space Environments Conference, AIAA-2016-3742, 2016, p. 3742.
[37] L. Bennani, P. Villedieu, M. Salaun, P. Trontin, Numerical simulation and modeling of ice shedding: process initiation, Comput. Struct. 142 (2014) 15–27.
[38] L. Bennani, Two dimensional modelling of electrothermal ice protection systems (Ph.D. thesis), Institut Supérieur de l'Aéronautique et de l'Espace (ISAE), 2014.
[39] D. Kintea, I. Roisman, C. Tropea, Transport processes in a wet granular ice layer: model for ice accretion and shedding, Int. J. Heat Mass Transfer 97 (2016) 461–472.
[40] E. Iuliano, E. Montreuil, E. Norde, E. Van der Weide, H. Hoeijmakers, Modelling of non-spherical particle evolution for ice crystals simulation with an eulerian

approach, in: SAE 2015 International Conference on Icing of Aircraft, Engines, and Structures, SAE 2015-01-2138, 2015.
[41] E. Ayan, S. Ozgen, C. Murat, E. Tarhan, Prediction of ice crystal accretion with TAICE, in: SAE 2015 International Conference on Icing of Aircraft, Engines, and Structures, SAE 2015-01-2148, 2015.
[42] A. Baumert, S. Bansmer, M. Bacher, Implementation of an innovative ice crystal generation and conveyance system to the icing wind tunnel Braunschweig, in: 53rd AIAA Aerospace Sciences Meeting and Exhibit, AIAA-2015-1225, 2015.
[43] A. Baumert, S. Bansmer, S. Sattler, H. Pervier, B. Esposito, Simulating natural ice crystal cloud conditions for icing wind tunnel experiments – a review on the design, commissioning and calibration of the TU Braunschweig ice crystal generation system, in: 8th AIAA Atmospheric and Space Environmehts Conference, AIAA 2016-4053, 2016.
[44] A. Baumert, Experimental and numerical studies on ice crystal icing of civil aircraft (Ph.D. thesis), Institute of Fluid Mechanics, Technische Universität Braunschweig (to be published in 2018).
[45] P. Trontin, A. Kontogiannis, G. Blanchard, P. Villedieu, Description and assessment of the new ONERA 2D icing suite IGLOO2D, in: 9th AIAA Atmospheric and Space Environments Conference, AIAA-2017-3417, Denver, USA, 2017.
[46] P. Trontin, P. Villedieu, A comprehensive accretion model for glaciated icing conditions, Int. J. Mult. Flow (2018) (under review).
[47] N. Haugen, S. Kragset, Particle impaction on a cylinder in a crossflow as function of Stokes and Reynolds numbers, J. Fluid Mech. 661 (2010).
[48] T. Currie, D. Fuleki, C. Davison, Simulation of ice particle melting in the NRC RATFac mixed-phase icing tunnel, in: SAE 2015 International Conference on Icing of Aircraft, Engines and Structures, 2015-01-2107, 2015.
[49] H. Traub, Experimental investigations of ice crystal icing of a heatable cylinder and wing model, Tech. rep., Student research project – Institute of Fluid Mechanics, TU Braunschweig, 2017.